Analysis, Design and Measurements of Flat and Curved Circularly Symmetric High Impedance Surfaces for Curvilinear Antenna Applications

by

Mikal Askarian Amiri

A Dissertation Presented in Partial
Fulfillment of the Requirements for
the Degree Doctor of Philosophy

Approved June 2018 by the
Graduate Supervisory Committee:

Constantine A. Balanis, Chair
James T. Aberle
Bertan Bakkaloglu
Georgios C. Trichopoulos

ARIZONA STATE UNIVERSITY

August 2018

ABSTRACT

In this dissertation a new wideband circular HIS is proposed. The circular periodicity made it possible to illuminate the surface with a cylindrical TEM^z wave and; a novel technique is utilized to make it wideband. Two models are developed to analyze the reflection characteristics of the proposed HIS.

The circularly symmetric high impedance surface is used as a ground plane for the design of a low-profile loop and spiral radiating elements. It is shown that a HIS with circular periodicity provides a wider operational bandwidth for curvilinear radiating elements such, such as loops and spirals, compared to canonical rectangular HISs. It is also observed that, with the aid of a circular HIS ground plane the gain of a loop and a spiral increases compared to when a perfect magnetic conductor (PMC) or rectangular HIS is used as a ground plane. The circular HIS was fabricated and the loop and spiral elements were placed individually in close proximity to it.

Also, due to the growing demand for low-radar signature (RCS) antennas for advanced airborne vehicles, curved and flexible HIS ground planes, which meet both the aerodynamic and low RCS requirements, have recently become popular candidates within the antenna and microwave technology. This encouraged us, to propose a spherical HIS where a 2-D curvature is introduced to the previously designed flat HIS.

The major problem associated with spherical HIS is the impact of the curvature on its reflection properties. After characterization of the flat circular HIS, which is addressed in the first part of this dissertation, a spherical curvature is introduced to the flat circular HIS and its impact on the reflection properties was examined when it was illuminated with the same cylindrical TEM^z wave. The same technique, as for the flat HIS ground plane, is utilized to make the spherical HIS wideband. A loop and spiral element were placed in the vicinity of the curved HIS and their performances

were investigated. The HISs were also fabricated and measurements were conducted to verify the simulations. An excellent agreement was observed.

To my beloved Family

ACKNOWLEDGMENTS

I would like to express my gratitude to Prof. Constantine A. Balanis for his expert tutoring and vigilant guidance throughout the course of my Ph.D. It is a great honor and an achievement for me to have worked with a Professor of his renown. I believe his skillful mentoring and attentive supervision shaped me into a technically skillful professional.

I would like to extend my thanks to the committee members Prof. James Aberle, Prof. Georgios Trichopoulos and Prof. Joseph C. Palais for their valuable suggestions and constructive criticisms.

It is a great pleasure to have worked with Craig R. Birtcher. His phenomenal work helped me to learn a lot about fabrication and measurements. I also thank him for his valuable inputs during the weekly meetings which were very productive.

My special thanks go to my family members who supported and encouraged me to pursue my dreams. I would not have accomplished my work without their sacrifice.

In addition, I would like to thank all my lab mates Dr. Ahmet Durgun, Dr. Alix Rivera-Albino, Dr. Nafati Aboserwal, Dr. Siva Pandi, Dr. Saud Saeed, Dr. Wengang Chen, Subramanian Ramalingam, Anuj Modi and Mohammed Al-Harbi for a pleasant environment and quality discussions.

This work was sponsored by ASU Industry-Government Advanced Helicopter Electromagnetics (AHE) Program.

TABLE OF CONTENTS

CHAPTER Page

LIST OF FIGURES

FIGURE Page

FIGURE Page

FIGURE Page

FIGURE Page

FIGURE Page

LIST OF TABLES

TABLE Page

Chapter 1

INTRODUCTION

Antenna designers have made immense advances in the past several decades. *High Impedance Surfaces (HISs)* or *Artificial Magnetic Conductors (AMCs)* are one of the breakthroughs that has emerged in modern antenna design, after they were first proposed in [1]. These surfaces are designed such that at a certain frequency the plane wave illumination is reflected with the same phase as that of the incident wave. This is in contrast to a perfect electric conductor (PEC) surface where a reflection phase of 180° is introduced to the phase of the incident wave. Thus, it can be concluded that HISs resemble the behaviour of perfect magnetic conductors (PMCs) within a certain bandwidth where the reflection phase is nearly zero.

1.1 Previous Work

The reflection properties of HISs have been extensively examined in [2], [3], [4], [5], [6]. Analytical models are also provided in [7], [8], [9], [10] to demonstrate the reflection characteristics of these surfaces. According to *image* theory, a horizontal radiating element cannot be placed in close proximity of a PEC ground plane, as the image of the source will be 180° out of phase which ultimately results in poor radiation. The horizontal element should be placed at a height of quarter of a wavelength above the conducting ground plane to attain maximum broadside radiation to the reflecting surface. The height can be reduced only if the image of the source is in the same phase (direction) as the actual source. To accomplish this, the ground plane has to be a perfect magnetic conductor. Although PMC materials do not exist in nature, HISs have similar reflection properties as PMC material, within a certain frequency

interval; i.e. a horizontal radiating element can be located in the vicinity of these type of artificial ground planes and yet radiate efficiently. Thus HISs are proper candidates to be used as antenna ground planes if a low-profile design is required. Various types of radiators, such as dipoles and curvilinear antennas, were placed in close proximity to these surfaces [11], [12], [13], [14]. HISs can also be utilized for antenna miniaturization and bandwidth enhancement [15], [16], [17]. The ideas of multiband and tunable HISs are discussed in [18], [19].

The other attractive property of these structures is surface wave suppression which also occurs within a specific frequency interval referred to as *Electromagnetic Band Gap (EBG)*. In [20], a planar EBG structure is used to reduce surface-wave losses for an aperture-coupled fed patch antenna on a thick high dielectric-constant substrate. A novel planar photonic band gap (PBG) scheme is presented in [21] for size reduction.

HIS structures are also utilized in designing reflectarray antennas with application in medical imaging [22], [23] and defect detection in dielectric materials [24]. A unit cell consisting of a ring loaded square patch with a varactor diode connected across the gap with nearly 180 degrees phase tenability was proposed in [25]. The unit cell was used to build a reflectarray antenna with +/- 60 degrees beam steering [26], [27].

Conformal and curved HISs have also recently received attention because of the growing demand for flexible structures. In [28], the reflection phase of a cylindrically curved HIS is characterized and an analytical model is developed.

Although most of the existing research focuses on rectangular surfaces, there are only a few investigations have been undertaken on curvilinear structures, the majority of which are focused on the EBG properties rather than HIS characteristics [29]. In [30], a planar circularly symmetric EBG structure is proposed to suppress the surface waves evenly in all directions. The radiation bandwidth of a printed slot surrounded by a circular EBG is then optimized in [31] and the proposed surface in [30] was

ultimately used to build a sector EBG antenna for high-directivity applications [32]. A dual-band circularly symmetric EBG substrate is also designed to improve the radiation properties of a dual-band circular patch antenna in [33]. In [34], the gain of a dielectric resonator antenna is improved by the utilization of a circular mushroom-like structure.

1.2 Scope of the Work

As mentioned above, the reflection characteristics and potential applications of a circularly symmetric HIS have not been addressed in depth in the existing literature. In this dissertation, we illustrate that curvilinear antenna elements have better performance above circular HISs rather than rectangular HISs. This superiority is mainly attributed to electric fields radiated by a circular loop antenna which interact more effectively with a circularly symmetric ground plane HIS.

The electromagnetic field expressions corresponding to a loop having an arbitrary current distribution is provided in [35]. These expressions show that the electric fields of a loop antenna with uniform current distribution ($C/\lambda << 1$ where C is the circumference of the loop) includes only the ϕ-component on the loop's plane. As the ratio of the circumference to the wavelength increases, the current becomes more non-uniform whose distribution causes the loop antenna to also generate a radial component. However, it would still be a valid approximation to neglect the small radial component and assume that the electric fields are mainly of azimuthal components on the plane of the loop. This approximation becomes more accurate as the radial distance increases. Making this assumption, it is shown in this dissertation that the figures-of-merit of a loop element can be enhanced by taking advantage of a HIS with circular symmetry (ϕ-direction periodicity).

Despite the performance enhancements of the loop antenna using a circular HIS

[36], these elements are generally narrowband radiators. In this dissertation, a spiral element is used, along with a circular HIS, to characterize the performance of wideband curvilinear radiating elements when placed above a circularly periodic ground plane [37], [38], [39]. Although a circular AMC reflector is used in [40] to improve the axial ratio of an archimedean spiral antenna (79% 2-dB axial ratio bandwidth), the major objective of this study is to broaden the fractional and operational bandwidths and also increase the broadside gain of spiral elements utilizing HIS ground planes with circular periodicity. The 3-dB axial ratio bandwidth is maintained at 11%, which is similar to the one in [41].

The main contributions of this dissertation are:

- Demonstrates that circularly symmetric HIS are superior ground planes for curvilinear antenna elements.
- Develops a fully analytical model which predicts the reflection characteristics of circular HISs when illuminated with cylindrical TEM^z waves.
- Illustrates that the operational bandwidth of curvilinear antenna elements placed above circular HISs are wider than those above rectangular HISs.
- Characterizes the phase profile of the circular HIS with which the electromagnetic waves of a loop antenna are reflected and having a constructive interference. This phenomenon increases the gain of a loop and spiral by 2.5 dB and 3 dB, respectively, compared with an ideal PMC ground plane.
- Illustrates that curvilinear elements have more symmetric elevation gain patterns.
- Illustrates that the same technique can be used to design a circular HIS with spherical curvature [42].

1.3 Outline of Dissertation

This dissertation is organized as follows. Chapter 2 covers the basic theory of HISs, their design procedure and also the challenges and strategies of designing a circular HIS. A method to make the circular HIS wideband is also presented in Chapter 2. Chapter 3 mainly concentrates on developing analytical models to characterize the reflection phase of circular HISs under normal incidence of cylindrical TEM^z wave. In Chapter 4, the performance of curvilinear radiating elements located above a circular HIS is examined in detail and compared for their performance when they are located above a rectangular HIS. A spherical curvature is introduced to the flat circular HIS of Section 2.2 and its impact on the reflection characteristics is examined. It is illustrated that the same basic principle of flat circular HIS can be used to make the spherical HIS wideband. Loop and spiral elements are placed, individually, above the spherical HIS and their performance is studied through simulations. Chapter 7 illustrates the fabrication and measurement procedure of the circular HIS, spiral and loop radiating elements and their feeding network. Measurements are presented and compared with simulations. Chapter 8 summarizes the conclusions and suggests some topics for future work.

Chapter 2

FLAT HIGH IMPEDANCE SURFACES

HISs are two-dimensional metamaterials which are commonly used as antenna ground planes for low-profile designs. As mentioned in Section 1.1, the majority of the current literature is focused on rectangular HISs. In Section 2.1, the theory and reflection characteristics of rectilinear HISs are reviewed. The strategies used to design a circular HIS are presented in Section 2.2.

2.1 Rectilinear HISs

HISs are generally realized by the periodic arrangement of metallic patches mounted on top of a grounded dielectric. Fig. 2.1 illustrates the 3-D CAD geometry of a rectangular HIS. Due to the *Floquet* Theorem, the reflection phase of a periodic structure can be obtained by simulating a single unit cell with the appropriate boundary conditions. Thus to obtain the phase of the reflection coefficient from the HIS of Fig. 2.1 under normal incidence of a plane wave, it is sufficient to find the reflection phase of the unit cell displayed in Fig. 2.2. It is obvious that

$$a = w + g \tag{2.1}$$

Fig. 2.3 illustrates typical reflection phase of a HIS under plane wave normal incidence. The frequency at which the reflection phase is 0° is defined as the resonant frequency.

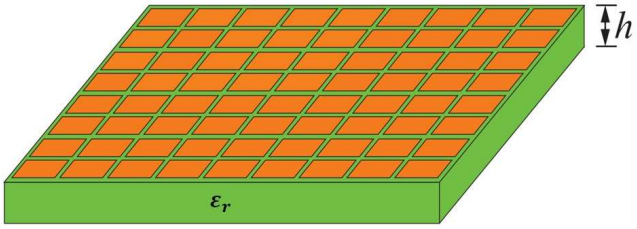

Figure 2.1: Geometry of a rectangular HIS with a substrate of height h and relative permittivity ϵ_r.

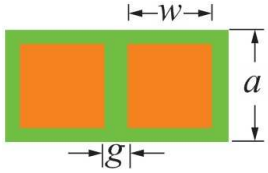

Figure 2.2: Geometry of two adjacent unit cells of the periodic structure of Fig. 2.1, with period of a, patch width of w and gap of g.

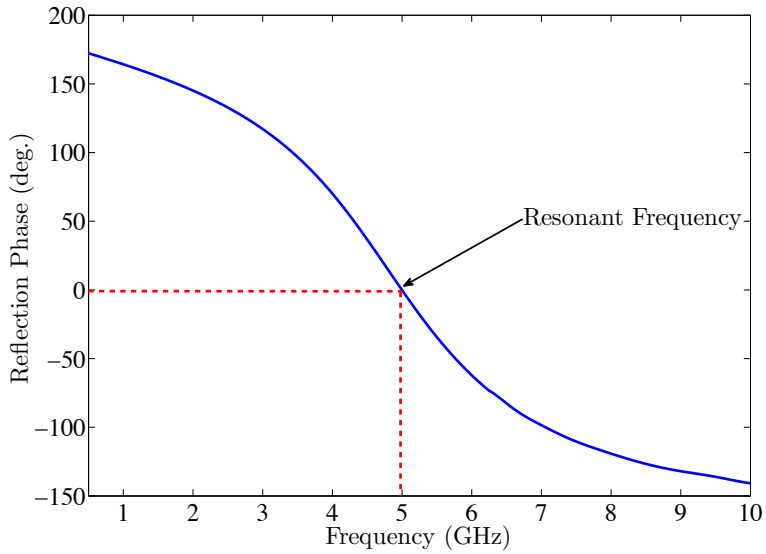

Figure 2.3: Reflection phase of the HIS of Fig. 2.1 with design parameters: $a = 1.2$ cm, $w = 0.8$ cm, $g = 0.4$ cm

2.2 Circular HISs

The circular HIS design considered in this dissertation is based on a Rogers RT/Duroid-5880 disc of thickness 0.635 cm whose bottom surface is covered with a copper sheet. The top surface of the dielectric is covered by circular rings that have periodic gaps in the angular direction. The angular design parameters are w_a and g_a, where w_a is the patch angle and g_a is the gap angle. The radial patch length and the radial gap length are represented by w_r and g_r, respectively. Thus, the unit cell design parameters are:

$$a_a = w_a + g_a \tag{2.2}$$

$$a_r = w_r + g_r$$

The surface with an angular periodicity is illustrated in Fig. 2.4. The angle of the unit cell (a_a) of this surface is 20°, the gap angle (g_a) is 6°, the radial length of the unit cell (a_r) is 2.22 cm, and finally, the radial gap length (g_r) is 0.9 cm. To illuminate the surface with a cylindrical TEM^z wave whose electric field is in the ϕ direction, it is required to simulate a coaxial cable with PMC boundary conditions on the surface of the inner and outer conductors, as was done in [29]. Fig. 2.5 illustrates the reflection phase diagram of the surface shown in Fig. 2.4 under normal incidence of cylindrical TEM^z wave illumination. As it can be observed from Fig. 2.5, the surface of Fig. 2.4 possesses many narrowband modes. Dividing the HIS of Fig. 2.4 into 4 single rings (Fig. 2.6) and simulating them individually illustrates that each ring is resonating at a different frequency, although all of the rings have the same design parameters; this is illustrated in Fig. 2.7. The interesting point is that the resonant frequency of each single ring is present in the reflection phase of the entire surface when all of the rings are placed together, as if the phase of the reflected wave from the entire surface is the superposition of the phases of the reflected waves from the single individual

rings. For instance, the 4^{th} ring of Fig. 2.6 is resonating at 3.74 GHz. This resonance is also observed in the reflection phase of the entire surface of Fig. 2.4 when the 4^{th} ring is placed next to the other rings. The same is true for all of the rings. There are still some other modes in the reflection phase of Fig. 2.4 which are attributed to the cross polarized component. This undesired component is introduced at the curved boundary of the metal patches and the dielectric. Since the cross polarized component is in the radial direction, its corresponding modes should be controlled by the size of the radial gaps.

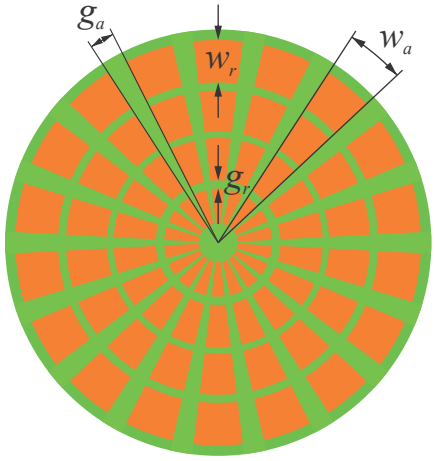

Figure 2.4: Top view of the HIS with an angular periodicity where $w_a = 14°$, $g_a = 6°$, $w_r = 2.22$ cm and $g_r = 0.9$ cm.

By changing the angular gaps, to achieve a wideband surface, all of the rings were designed to resonate at the same frequency. The cross polarized modes are also shifted to higher frequencies by changing the radial gaps. Using these two guidelines, a circularly symmetric surface was designed with a zero reflection phase at 4.5 GHz. To achieve such a geometry, the gap angle of the first ring was decreased from 6° to 1° but the gap angles of all other rings were increased. The radial length of the patches were then adjusted to shift the cross polarized modes to out of band. The unit cells of

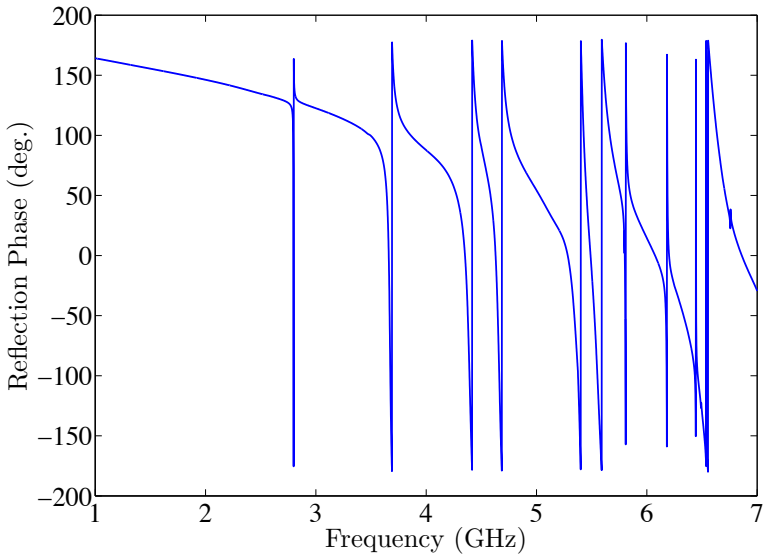

Figure 2.5: Reflection phase of the surface of Fig. 2.4 under illumination by a cylindrical TEM^z wave.

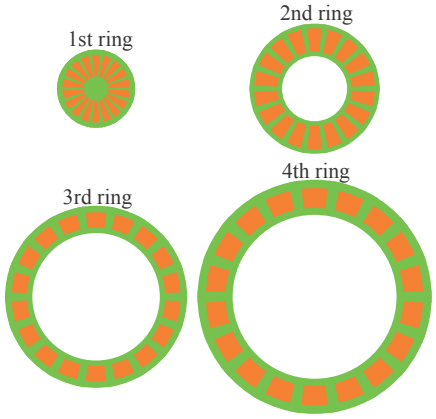

Figure 2.6: Separate ring configuration of Fig. 2.4.

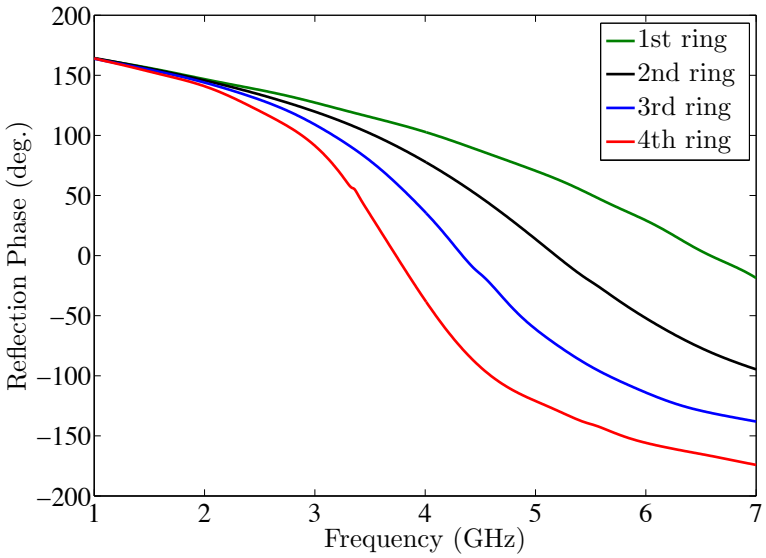

Figure 2.7: Reflection phase of each single ring of Fig. 2.6.

all of the rings have an angle of 20° and a radial width of 2.22 cm. Design parameters are summarized in Table 2.1. Fig. 2.8 displays the reflection phase of each single ring and also the reflection phase of the entire surface when all the rings are present. It is implied from Table 2.1 and Fig. 2.8 that a wideband surface has different design parameters on each ring. Although the unit cell's angle and radial width of each ring is maintained constant through the design procedure, the geometry of the patches (w_a and w_r) of each ring is different from the other ones.

Table 2.1: Design parameters of circular HIS with the zero reflection phase at 4.5 GHz.

Parameter	g_a (deg)	g_r (cm)
1^{st} ring	1	1.35
2^{nd} ring	6.6	1.1
3^{rd} ring	8.4	1.1
4^{th} ring	9.5	1.2

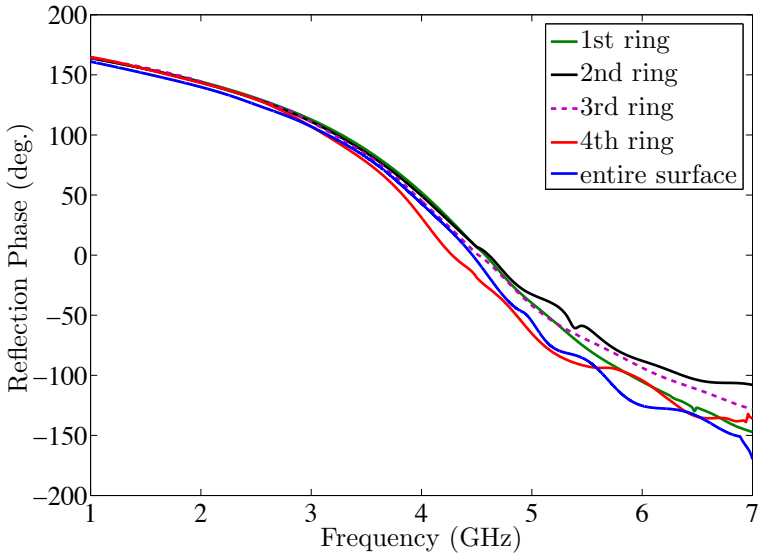

Figure 2.8: Reflection phase of the single rings and the combined surface with resonant frequency of 4.5 GHz.

Chapter 3

ANALYTICAL MODELING OF FLAT CHIS

In this Chapter, two models, the *quasi-static* and *wideband*, are developed to analyze the reflection characteristics of the circularly symmetric HIS. Based on the *Floquet theorem*, the reflection phase of a periodic structure is the same as the reflection phase of a single unit cell if appropriate boundary conditions are applied. Thus unit cells are used to find the surface impedance of each ring. The surface impedance of single rings are then combined to find the surface impedance of the entire structure. The numerical results of both models, along with the full-wave simulation data, are shown and compared with each other in the last part of this Chapter.

3.1 Quasi-Static Model

The idea of the *quasi-static* model is based on finding the equivalent surface impedance of a unit cell in terms of lumped capacitances and inductances that are in parallel with each other[1]. The capacitance is mainly due to the fringing effect of the patch edges and the inductance is attributed to the grounded substrate. From the theory of conformal mapping, the electric flux density of a pair of semi-infinite conducting plates separated by a gap of width g and a voltage difference of V_0 is [43]:

$$\Psi = \mathrm{Im}\left[\frac{\epsilon V_0}{\pi}\cos^{-1}\left(\frac{x+iy}{g/2}\right)\right] \tag{3.1}$$

For two finite plates with widths of w as illustrated in Fig. 3.1 when $w >> g$, the flux ending on the plates can be approximated by:

$$\Psi = \frac{2\epsilon V_0}{\pi}\cosh^{-1}\left(\frac{w+g}{g}\right) \tag{3.2}$$

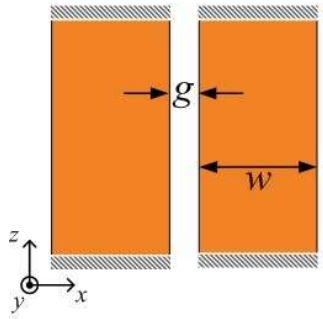

Figure 3.1: Geometry of two finite plates separated by a small gap of width g.

Since the gap width between the plates is constant in the z-direction, the electric flux density is not changing with respect to z and the capacitance per unit length is only a function of the ratio w/g. Thus the total fringing capacitance between two finite plates is equal to the capacitance per unit length times the length of the patch in the z-direction. For a square patch mounted on top of a dielectric with permittivity of ϵ_r the edge capacitance is given by [1]:

$$\begin{aligned} C &= \text{capacitance per unit length} \times \text{patch length} \\ &= \frac{w\epsilon_0(1+\epsilon_r)}{\pi}\cosh^{-1}\left(\frac{w+g}{g}\right) \end{aligned} \tag{3.3}$$

which is valid if the flux function is not varying with respect to the direction parallel to the edges of the plate. However, in the geometry of Fig. 3.2, the electric flux density is a function of the radial direction as well. Although (3.2) can still be used to model the angular behavior of the flux at a constant ρ in the ϕ-direction, the radial dependence of the flux function must be modeled. This can be approximated with the behavior of the electric flux density between two semi-infinite conducting planes intersecting at an angle of α, but separated by an infinitesimal gap at the origin so that the plane at $\phi = 0$ may be placed at zero potential, and the plane at $\phi = \alpha$ at

potential V_0, as illustrated in Fig. 3.3.

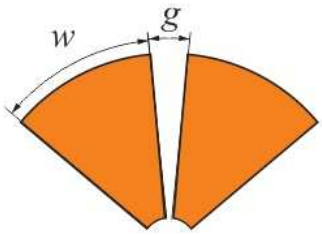

Figure 3.2: Geometry of the patches of the circular HIS with patch angle of w and gap angle of g.

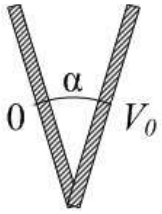

Figure 3.3: Geometry of the semi-infinite conducting planes intersecting at an angle of α .

The flux function of the geometry of Fig. 3.3 is given by (3.4) where ρ_1 is the flux function's reference. From (3.4), it can be concluded that the electric flux can be modeled as a logarithmic function along the radial direction.

$$\Psi(\rho) = \frac{V_0}{\alpha}\ln\left(\frac{\rho}{\rho_1}\right) \tag{3.4}$$

It is concluded from (3.4) that the electric flux variation of Fig. 3.3 with respect to radius should be modeled as $\frac{1}{g}\ln(\rho)$. Thus the flux function ending on the plates of Fig. 3.2 is

$$\Psi(\rho) = \frac{2\epsilon V_0}{\pi g}\cosh^{-1}\left(\frac{w+g}{g}\right)\ln\left(\frac{\rho}{\rho_1}\right) \tag{3.5}$$

To find the total charge between the patches of Fig. 3.2, the flux ending on one patch needs to be found. This can be obtained by integrating it from ρ_1 to ρ_2, which are the inner and outer radii of the patches, respectively. This value is equal to the product of the capacitance and the voltage across the metallic patches; hence it should be divided by V_0. Therefore, the total capacitance of the patches of Fig. 3.2, when they are mounted on top of a dielectric with the relative permittivity of ϵ_r, is given by:

$$C = \frac{\epsilon_0(1+\epsilon_r)}{\pi}\cosh^{-1}\left(\frac{w+g}{g}\right)\left[\rho_2 \ln\left(\frac{\rho_2}{\rho_1}\right) - \rho_2 + \rho_1\right] \tag{3.6}$$

The equivalent inductance of the grounded dielectric with the permeability of μ under cylindrical TEM^z wave illumination is equal to [1]:

$$L = \mu h \tag{3.7}$$

To obtain the surface impedance of each ring, the capacitor and inductor values from (3.6) and (3.7) should be used in (3.8), which is the input impedance of the parallel LC circuit.

$$Z_{eq} = \frac{j\omega L}{1-\omega^2 LC} \tag{3.8}$$

3.2 Wideband Model

The basic idea of the *wideband* model is to consider the impact of the higher order modes that can propagate within the waveguide being used for the unit cell simulation, which in our case is a cross section of a cylindrical waveguide (an annular sector with inner and outer radii of ρ_1 and ρ_2, respectively). Fulfilling this purpose, the impedance of different modes of the incident wave on the unit cell and their

corresponding reflected and transmitted waves are found separately, and appropriate coefficients are used to obtain the weighted sum of the impedance of all of the modes. Hence, the impact of all of the modes is taken into account with a certain weight in the final expression of the surface impedance. This makes the model more accurate, especially beyond the *quasi-static* frequency ranges. Fig. 3.4 shows the unit cell geometry and the appropriate boundary conditions on the waveguide walls. The equivalent transmission-line model is also illustrated in Fig. 3.4.

To obtain the impedance of the different modes, we should solve the wave equation within the unit cell waveguide of Fig. 3.4. The vector potential within a cross section of a cylindrical waveguide shown in Fig. 3.4(a), for the TE^z mode, is

$$F_z = [A_1 J_m(\beta_\rho \rho) + B_1 Y_m(\beta_\rho \rho)]\cos(m\phi)e^{-j\beta_z z} \tag{3.9}$$

where the eigenvalues can be obtained from

$$J_m(\beta_\rho \rho_1)Y_m(\beta_\rho \rho_2) - J_m(\beta_\rho \rho_2)Y_m(\beta_\rho \rho_1) = 0 \tag{3.10}$$

$$m = \frac{n\pi}{a}$$

$$n = 1, 2, 3, ...$$

The transverse components of the electric field are

$$E_\phi = \frac{\beta_\rho \rho}{\epsilon}[A_1 J_m^{'}(\beta_\rho \rho) + B_1 Y_m^{'}(\beta_\rho \rho)]\cos(m\phi)e^{-j\beta_z z} \tag{3.11}$$

$$E_\rho = \frac{n\pi}{\epsilon a \rho}[A_1 J_m(\beta_\rho \rho) + B_1 Y_m(\beta_\rho \rho)]\sin(m\phi)e^{-j\beta_z z} \tag{3.12}$$

For the TM^z modes the vector potential is

$$A_z = [A_1 J_m(\beta_\rho \rho) + B_1 Y_m(\beta_\rho \rho)]\sin(m\phi)e^{-j\beta_z z} \tag{3.13}$$

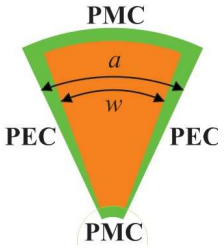

(a)

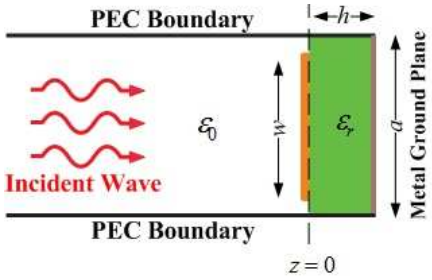

(b)

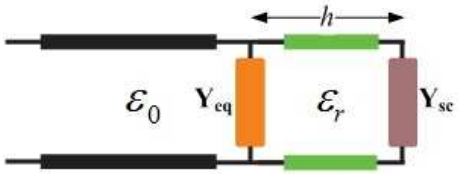

(c)

Figure 3.4: (a) Top view of the unit cell geometry. (b) Side view of the unit cell geometry. (c) Transmission-Line model of the unit cell.

where the eigenvalues can be obtained from

$$J_m^{'}(\beta_\rho\rho_1)Y_m^{'}(\beta_\rho\rho_2) - J_m^{'}(\beta_\rho\rho_2)Y_m^{'}(\beta_\rho\rho_1) = 0 \tag{3.14}$$

$$m = \frac{n\pi}{a}$$

$$n = 0, 1, 2, ...$$

The transverse components of the electric field are

$$E_\phi = \frac{-n\pi\beta_z}{\omega\mu\epsilon\rho a}[A_1 J_m(\beta_\rho\rho) + B_1 Y_m(\beta_\rho\rho)]\cos(m\phi)e^{-j\beta_z z} \tag{3.15}$$

$$E_\rho = \frac{\beta_\rho\beta_z}{\omega\mu\epsilon}[A_1 J_m^{'}(\beta_\rho\rho) + B_1 Y_m^{'}(\beta_\rho\rho)]\sin(m\phi)e^{-j\beta_z z} \tag{3.16}$$

For both TE^z and TM^z modes, β_z is represented by

$$\beta_z = \sqrt{\omega^2\mu\epsilon - \beta_\rho^2} \tag{3.17}$$

Since the electric field expressions of (3.11) and (3.15) are periodic functions of ϕ, they can be expanded in a Floquet series of spatial harmonics. Thus the transverse electric field in Fig. 3.4(b) at $z = 0$ can be expanded as [44]

$$E(\rho, \phi) = 1 + \Gamma + \sum_{n=-\infty}^{+\infty} E_n(\rho)e^{-jn\phi} \tag{3.18}$$

where the amplitude of the incident wave is unity and Γ is the reflection coefficient of the first harmonic. Assuming that the substrate shown in Fig. 3.4(b) is not backed by the metallic ground plane and it is extended towards infinity in the z-direction, the transverse magnetic fields in free space (ϵ_0) and the substrate (ϵ_r) are

$$H^{(0)}(\rho, \phi) = Y_1^{(0)}(1 - \Gamma) - \sum_{n=-\infty}^{+\infty} Y_n^{(0)} E_n(\rho)e^{-jn\phi} \tag{3.19}$$

$$H^{(r)}(\rho, \phi) = Y_1^{(r)}(1 - \Gamma) - \sum_{n=-\infty}^{+\infty} Y_n^{(r)} E_n(\rho)e^{-jn\phi} \tag{3.20}$$

where $Y_n^{(0)}$ and $Y_n^{(r)}$ are the wave admittance in free space and substrate, respectively. The total equivalent admittance of each ring, which is represented by Y_{eq} in Fig. 3.4(c), is then obtained in terms of $Y_n^{(0)}$ and $Y_n^{(r)}$. Next, two cases are considered. In the first case the gap angle is much smaller than the patch angle ($g << w$), while in the second case the gap angle is comparable to the patch angle ($g \approx w$).

3.2.1 Case for which $g << w$

To find Y_{eq}, the Floquet series coefficients of the electric field over the gap should be found. From Fourier series analysis, the coefficients of the zeroth and higher order harmonics of (3.18) are given by

$$1 + \Gamma = \frac{1}{a}\int_0^g E_g(\rho,\phi)d\phi = \frac{1}{a}\tilde{E}_g(\rho,0) \tag{3.21}$$

$$E_n(\rho) = \frac{1}{a}\int_0^g E_g(\rho,\phi)e^{jn\phi}d\phi = \frac{1}{a}\tilde{E}_g(\rho,n) \tag{3.22}$$

where E_g represents the electric field over the gap and $\tilde{E}_g$ represent the n^{th} spatial harmonic. Using (3.21) and (3.22), E_n can be related to the electric field spatial harmonics as

$$E_n = (1+R)\frac{\tilde{E}_g(n)}{\tilde{E}_g(0)} \tag{3.23}$$

and from the continuity of the magnetic field through the gap, the reflection coefficient can be written as [44]

$$\Gamma = \frac{Y_0^{(0)} - Y_0^{(r)} - Y_{eq}}{Y_0^{(0)} - Y_0^{(r)} + Y_{eq}} \tag{3.24}$$

where

$$Y_{eq} = \sum_{n=-\infty}^{\infty} \left|\frac{\tilde{E}_g(n)}{\tilde{E}_g(0)}\right|^2 \left[Y_n^{(0)} + Y_n^{(r)}\right] \tag{3.25}$$

Equation (3.25) represents the total equivalent admittance of Fig. 3.4 assuming that the substrate is infinite and not backed by a PEC surface. To obtain the surface

admittance of the circular HIS, the impact of the metallic ground plane has to be taken into account. This is reflected in the transmission line model of Fig. 3.4(c) as Y_{sc}. Hence, $Y_n^{(r)}$ in (3.25) should be replaced by $-jY_n^{(r)}\cot(\beta_n^{(r)}h)$ due to transmission line theory, and the surface admittance of the unit cell shown in Fig. 3.4 becomes

$$Y_{eq} = \sum_{n=-\infty}^{\infty} \left| \frac{\tilde{E}_g(\rho, n)}{\tilde{E}_g(\rho, 0)} \right|^2 \left[Y_n^{(0)} - jY_n^{(r)}\cot(\beta_n^{(r)}h) \right] \tag{3.26}$$

All of the terms in (3.26) are easy to compute except for the ratio of the zeroth to the higher spatial harmonic of the electric field over the gap which can only be computed if the electric field profile of the gap is known. Therefore, it is necessary to find an expression for the electric field distribution over the gap.

The electric field profile over an electrically small slit with a constant width is of Maxwellian distribution [45]. Although the gap width between the patches of a single ring increases in the radial direction, Maxwell's distribution used in [44] can be modified such that the electric field profile expression includes the radial variation. Fig. 3.5 shows the electric field intensity along two arcs with different radii under TE^z incidence. As can be seen, the electric field profile on both arcs is of Maxwellian distribution with respect to ϕ; however, its intensity is inversely proportional to the radius of the arc. Thus, we propose (3.27) to be used as the field profile over the gap

$$E_g(\rho, \phi) = Ah(\rho)f(\phi) \tag{3.27}$$

where A is a frequency-dependent coefficient, $h(\rho)$ is given by

$$h(\rho) \propto \frac{1}{\rho} \tag{3.28}$$

and $f(\phi)$ for TE/TM polarizations are, respectively, given by

$$f_{TE}(\phi) \propto \left[1 - \left(\frac{2\phi}{g} \right)^2 \right]^{\frac{1}{2}} \tag{3.29}$$

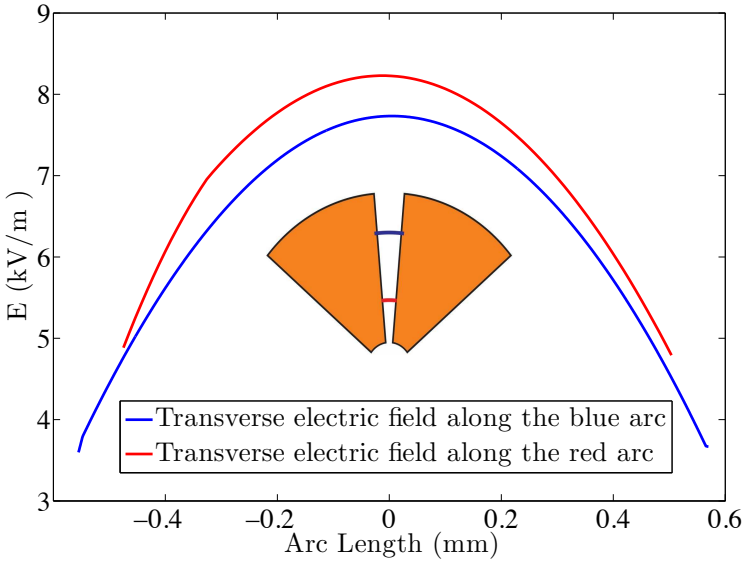

Figure 3.5: Transverse electric field distribution along two arcs over the gap at 4 GHz.

Table 3.1: Electric field expressions for different polarizations and their spatial harmonics

Polarization	$E_g(\rho, \phi)$	$\tilde{E}_g(\rho, n)$
TE	$A\frac{1}{\rho}\left[1-(\frac{2\phi}{g})^2\right]^{\frac{1}{2}}$	$A\frac{1}{\rho}J_0(\frac{ng}{2})$
TM	$A\frac{1}{\rho}\left[1-(\frac{2\phi}{g})^2\right]^{-\frac{1}{2}}$	$A\frac{1}{\rho}\frac{J_1(\frac{ng}{2})}{\frac{ng}{2}}$

$$f_{TM}(\phi) \propto \left[1 - \left(\frac{2\phi}{g}\right)^2\right]^{-\frac{1}{2}} \tag{3.30}$$

Table 3.1 summarizes the gap's electric field distribution and its spatial harmonics with respect to the polarization. Using $\tilde{E}_g$, provided in Table 3.1, in (3.26) to find the ratio of the n^{th} harmonics to the zeroth harmonic, Y_{eq} reduces to

$$Y_{eq} = \sum_{n=-\infty}^{\infty} \left|\frac{\tilde{f}(n)}{\tilde{f}(0)}\right|^2 \left[Y_n^{(0)} - jY_n^{(r)}\cot(\beta_n^{(r)}h)\right] \tag{3.31}$$

As can be seen in (3.31), the ratio of n^{th} harmonics to the zeroth harmonic is independent of the radial variation, although it was taken into account in (3.27).

3.2.2 Case for which $g \approx w$

For the case of the wider gaps whose geometry is illustrated in Fig. 3.6, the current distribution on the patch is considered instead of the electric field over the gap [44]. The current density on the patches is equal to the discontinuity of the tangential magnetic field

$$J_s(\rho, \phi) = H^{(0)}(\rho, \phi) - H^{(r)}(\rho, \phi) \tag{3.32}$$

Using the magnetic field expressions of (3.19) and following the same procedure as

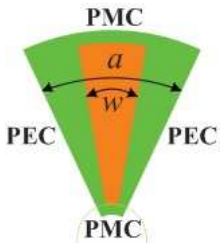

Figure 3.6: Geometry of the unit cell where the gap angle is comparable to the patch angle.

was done for the electric field in the case of the narrow gaps, it can be shown that

the equivalent impedance of the surface with wider gaps is

$$Z_{eq} = \sum_{n=-\infty}^{\infty} \left| \frac{\tilde{f}(n)}{\tilde{f}(0)} \right|^2 \frac{1}{Y_n^{(0)} - jY_n^{(r)} \cot(\beta_n^{(r)} h)} \tag{3.33}$$

3.3 Numerical Results and Comparison of the Methods

Fig. 3.7 illustrates the reflection phase of the 1^{st} and the 4^{th} ring obtained from both of the proposed analytical models and HFSS. For the *quasi-static* model, we used (3.3), (3.7) and (3.8) to find the surface impedance of each ring. In the *wideband* model, (3.31) is used to obtain the surface impedance of the 1^{st} ring where the gaps are very small and (3.33) is used to obtain that of the 4^{th} ring as the gaps are wider. Although an infinite number of terms are required to compute the impedance from the equations of the *wideband* model, we only used the modes whose cutoff frequencies were within the frequency range of interest. As it can be seen in Fig. 3.7, the reflection phase from both of the models are in good agreement with the results from the full-wave simulation for the first ring. For the 4^{th} ring, the results from the *wideband* model are pretty close to the full-wave simulation; however, the *quasi-static* model results are very different from the other two. Inaccurate results of the *quasi-static* model for the fourth ring can be attributed to the assumption of very narrow gap that was made in the derivation of the edge capacitance. However, the *quasi-static* model can help the designers to make some initial starting values of the design parameters (gap and patch angle) as it is more straightforward.

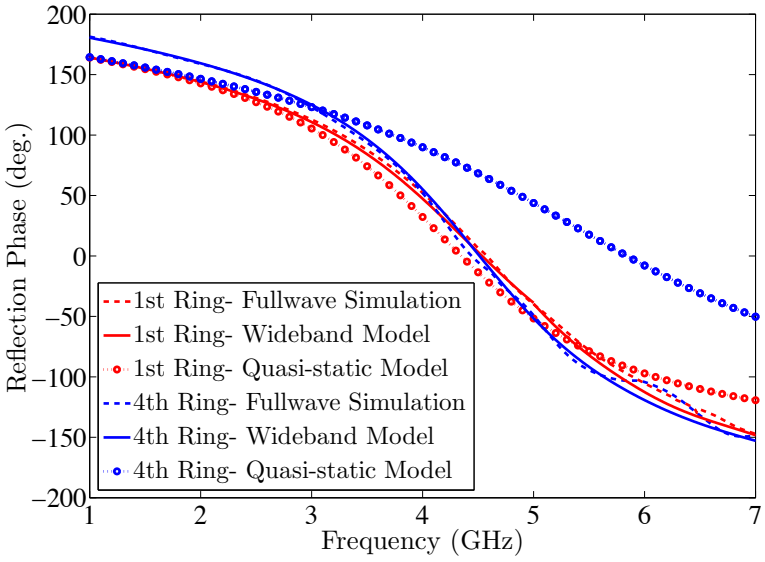

Figure 3.7: Reflection phase diagram of the 1^{st} and 4^{th} ring obtained by the proposed models and HFSS.

Chapter 4

ANTENNA APPLICATIONS OF FLAT CIRCULAR HIS (CHIS)

As it was mentioned in Section 1.1, circular HISs may serve as superior ground planes, than rectangular HISs, for curvilinear radiating elements, such as a loop. In this Chapter two curvilinear elements (loop and spiral) are placed above the circular HIS of Chapter 2 and their radiation characteristics are examined and compared with those above the rectangular HIS.

4.1 Loop Element

4.1.1 Operational Bandwidths

Fig. 4.1 illustrates the geometry of a loop element placed in the vicinity of the circular HIS. To obtain the operational bandwidth of the circular HIS, the radius of the loop was varied. The frequency interval over which the return loss is below -10 dB is the operational bandwidth of the circular HIS [11]. Assuming a center frequency of 3 GHz, the loop antenna is located at 0.01λ above the ground plane. Fig. 4.2 exhibits the return losses of loops with different radii, and the data indicate that the -10 dB operational bandwidth of the surface for loop antenna is about 37% at 3 GHz.

To compare the operational bandwidth of the circular HIS to that of the rectangular HIS, a loop was placed at the same height above the rectangular HIS which has an equal surface area and also an identical reflection characteristic as the circular HIS. Fig. 4.3(a) illustrates the geometry of a rectangular HIS with a unit cell size of 2 cm and square patches with side length of 1.36 cm. The thickness and electrical properties of the substrate are also the same as those of the substrate of the circular HIS. As it can be seen in Fig. 4.3(b), the reflection characteristic of both HISs are

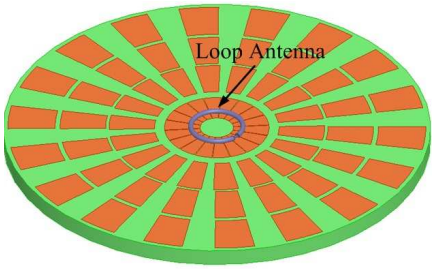

Figure 4.1: 3D CAD geometry of a loop antenna at a height of 0.01λ above a circular HIS.

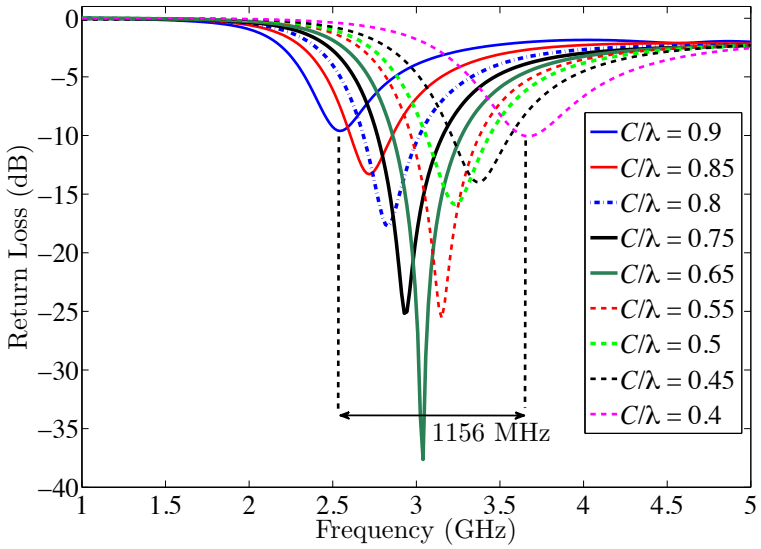

Figure 4.2: Return losses of the loop antennas with different radii located above the circular HIS.

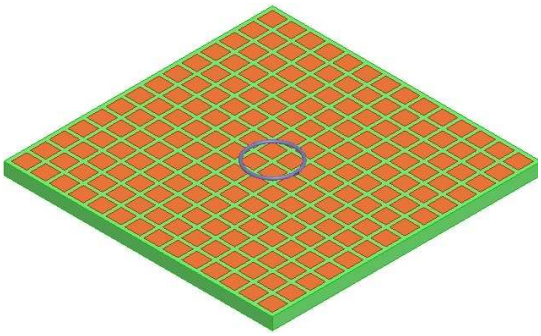

(a)

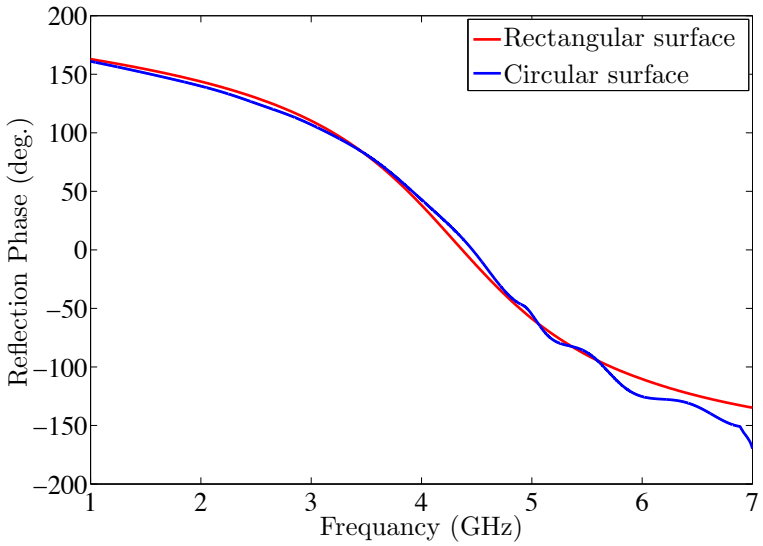

(b)

Figure 4.3: (a) 3D CAD geometry of a loop antenna at a height of 0.01λ above the rectangular HIS. (b) Reflection phase of the rectangular HIS under normal TEM illumination.

almost identical. Following the same procedure to obtain the operational bandwidth, simulations indicated that the -10 dB bandwidth of the rectangular HIS is about 26% (versus 37% for the circular HIS). Fig. 4.4 illustrates the return losses of loops antennas with different radii placed above the rectangular HIS.

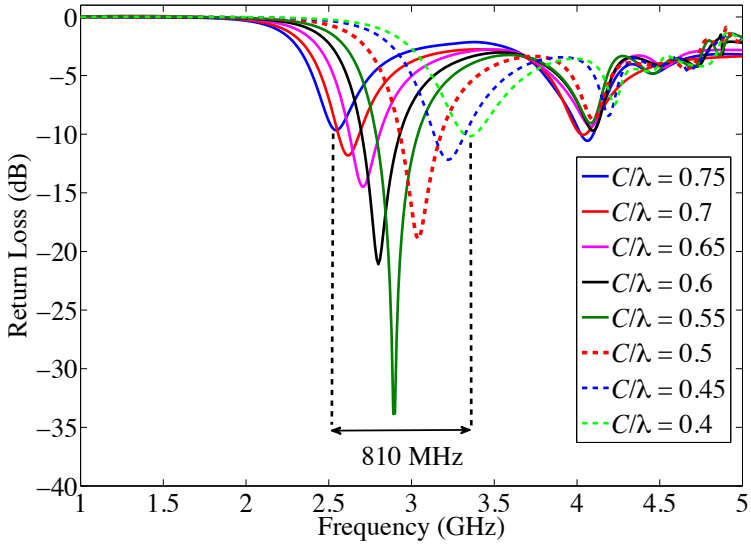

Figure 4.4: Return losses of the loop antennas with different radii located above the rectangular HIS.

4.1.2 Gain Pattern

For further comparisons, the gain pattern of a loop of radius 1 cm above the circular and rectangular HIS is obtained at 3 GHz. As it can be seen in Fig. 4.5 the gain pattern of the loop antenna is more symmetric on different elevation planes when it is placed above the circular HIS.

The gain of a loop with a radius of 1 cm at 3 GHz in free space is slightly greater than 2 dB [46] and due to *image* theory, it increases by 3 dB when it is located above an ideal PMC surface. In the case of the rectangular HIS, the gain increases from 2 dB to 5.5 dB. However, if the loop is placed above a circular HIS, the gain increases by 6 dB which makes the total gain 8.5 dB. To justify the extra 3 dB increase in the gain, it would be helpful to look at the phase with which the electric field of the loop is reflected from different parts of the HIS ground plane. It should be noted that,

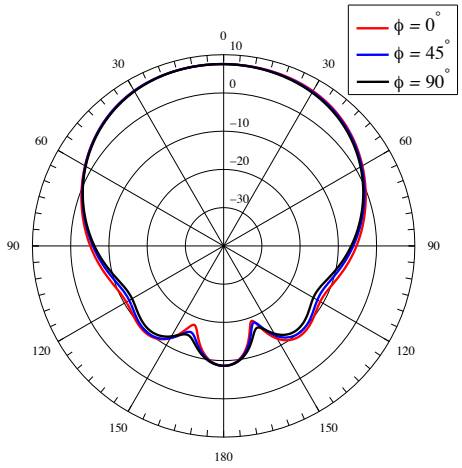

(a)

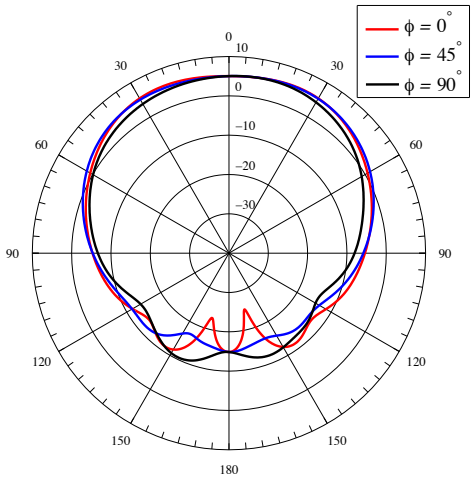

(b)

Figure 4.5: Gain of the loop antenna on different ϕ planes when it is located above: (a) circular HIS (b) rectangular HIS.

although the unit cell geometry of each ring is adjusted such that all of the rings have identical reflection phases under normal illumination of cylindrical TEM^z wave,

the rings do not necessarily have the same reflection characteristics under oblique illumination. On the other hand, the problem of a localized source (loop element) is different from the problem of normal plane wave illumination. When a loop antenna is located in the vicinity of the circular HIS, the angle of incidence increases as the point of reflection increases in the radial direction. As illustrated in Fig. 4.6(a), the incidence angle of the waves radiated by the loop can be considered as normal only within the inner portion (the area directly beneath the loop) of the surface; hence, the reflection phase of this portion of the surface can be approximated as the reflection phase of the circular HIS of Fig. 2.4, when it is illuminated by cylindrical TEM^z waves. Such an approximation cannot be made for the outer portion of the surface (which is not beneath the loop) as the waves radiated by the localized source impinge on the surface at oblique angles. This is also illustrated in Fig. 4.6(a). Thus, the reflection phase of the outer portion of the surface under the illumination of the localized source has to be observed separately. Fulfilling this purpose, it is sufficient to observe the phase of the tangential component of the electric field along a radial line as the surface is symmetric in the ϕ-direction. Fig. 4.6(c) displays the reflection phase of the electric fields radiated by the loop along the dotted line of Fig. 4.6(b). The changes in the reflection phase of the electric fields of the localized source in the radial ρ-direction is attributed to the:

- Incident angle of the radiated wave by the localized source that changes with respect to ρ.
- Impedance of the surface that changes with respect to ρ, due mainly to the texture of the surface which varies in the radial direction.

The reflection phase variation along the dotted radial line of Fig. 4.6(a) is such that causes a constructive phase interference in the broadside direction, which ul-

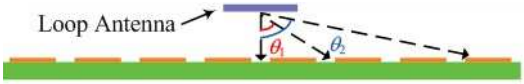

(a)

(b)

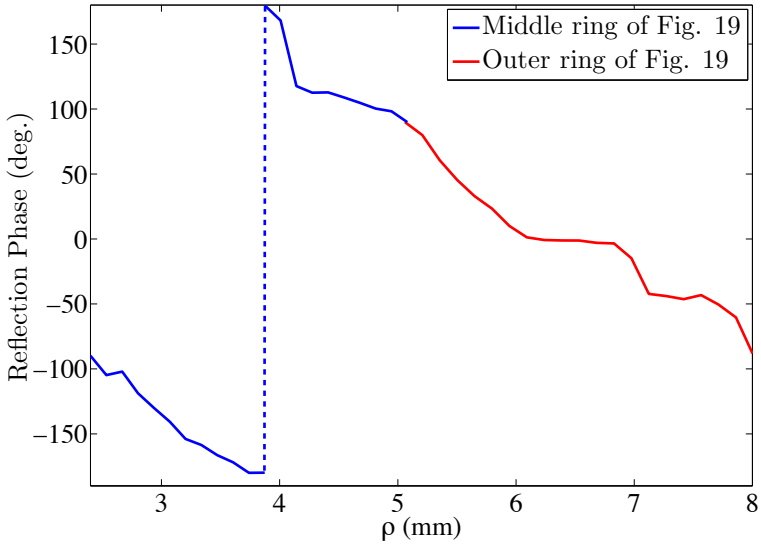

(c)

Figure 4.6: (a) Oblique incidence angle of the electromagnetic wave radiated by a loop antenna (b) Side view of the circular HIS with a loop antenna above it (c) Reflection phase of the electric field radiated by the loop antenna at 3 GHz along the dashed line shown in Fig. 4.6(b).

timately results in a higher gain compared with an ideal PMC where the surface impedance is neither a function of the incident angle nor a function of the point of reflection.

One way to validate that the high gain of the loop antenna above the circular HIS

is due to the different reflection phases, introduced to the electromagnetic waves of the localized source on different spots, is to synthesize the surface impedance of the circular HIS such that the synthesized surface has the same radial reflection phase profile as the circular HIS, when it is illuminated by a loop. To accomplish this, the surface is divided into three rings and the surface impedance of each ring is determined based on the reflection phase of Fig. 4.6(c). As mentioned earlier, it can be assumed that the electromagnetic waves of the loop impinge on the inner ring (green zone) of the surface at right angle; thus, (4.1) can be used to find its corresponding surface impedance.

$$\Gamma_1 = \frac{\eta_1 - \eta_0}{\eta_1 + \eta_0} = 1e^{j\phi_1} \tag{4.1}$$

In (4.1), Γ_1 is the complex reflection coefficient with the magnitude of unity and phase of ϕ_1, η_0 is the wave impedance of the free space and η_1 is the surface impedance of the inner ring of the surface of Fig. 4.7. In order to obtain η_1 from (4.1), it is only required to find the appropriate ϕ_1 of Γ_1, since its magnitude is equal to unity. As discussed before, Γ_1 can be approximated to be the same as the reflection coefficient of the surface under normal illumination of cylindrical TEM^z wave; hence, ϕ_1 at 3 GHz can be obtained from Fig. 2.8 which would be equal to 90°.

Next, the surface impedance of the middle and outer rings (blue and red zones) of Fig. 4.7 should be found; however, (4.1) cannot be used anymore since it is valid for normal incidence only. As the ratio of the circumference of the loop to the wavelength at 3 GHz is very small, it can be assumed that the electric field of the waves radiated by the loop antenna is only of ϕ-component. Therefore the configuration of the oblique incident wave on the surface on a constant elevation ϕ plane can be considered to be the same as the TE configuration of [14] and [47]. For the TE incident wave the

reflection coefficient is given by

$$\Gamma_i = \frac{\eta_i - \eta_0 \cos\theta_i}{\eta_i + \eta_0 \cos\theta_i} = 1e^{j\phi_i} \tag{4.2}$$

where θ_i is the incident angle.

To obtain the surface impedance of the middle or the outer ring from (4.2), it is only required to find the phase (ϕ_i) of the reflection coefficient as the magnitude of Γ_i is unity; ϕ_i for each of the rings of Fig. 4.7 is approximated as the average of the reflection phase given in Fig. 4.6(c) along the radial direction. The average reflection phases of the middle ring (2.4 cm $< \rho <$ 5.2 cm) and the outer ring (5.2 cm $< \rho <$ 8 cm) are 180° and 5° respectively. The averaged reflection phases of the ring sections are then substituted in (4.2) and the surface impedances are found accordingly.

The equivalent surface impedances assigned to inner, middle and outer rings are -$j377$, 0 and $j1750$ Ω/m^2, respectively. Fig. 4.8 illustrates the gain pattern of the same loop placed above the synthesized surface, which is very close to that of the loop antenna above the circular HIS. The pattern obtained from the synthesized surface can be even more accurate by subdividing the surface to more rings of smaller radial width.

So far, it has been shown that the broadside gain of the loop antenna at 3 GHz is higher when it is located above the circular HIS. To investigate if the same constructive phase interference happens over the entire operational bandwidth, the broadside gain of the loop antenna was simulated vs. frequency. Fig. 4.9 displays the gain of the loop antenna; it is evident that, within the frequency range of interest, the gain is higher when the loop is located above the circular HIS rather than the rectangular one.

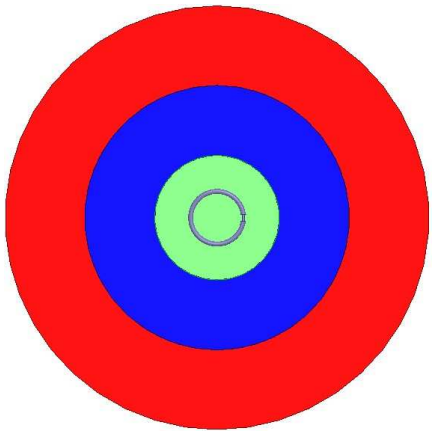

Figure 4.7: Top view of the synthesized surface divided into three impedance sections and a loop antenna above it.

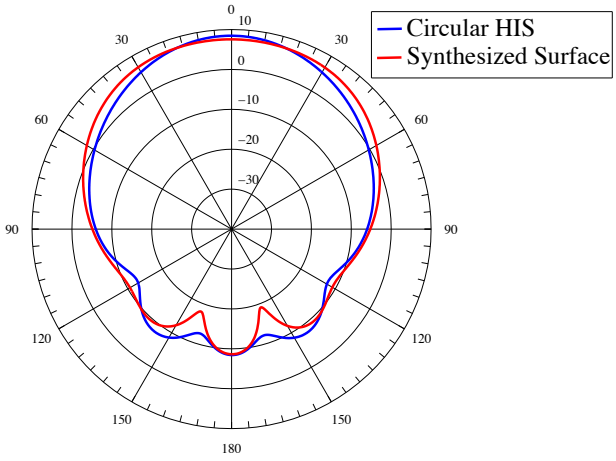

Figure 4.8: Gain pattern of a loop antenna above the circular HIS of Fig. 4.1 and the synthesized surface of Fig. 4.7 at 3 GHz.

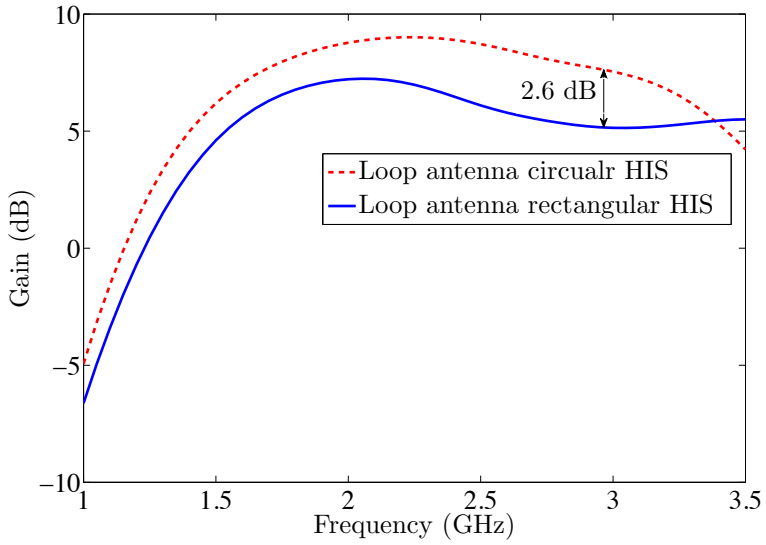

Figure 4.9: Broadside gain of the loop antenna above the circular HIS.

4.2 Spiral Element

4.2.1 Operational and Fractional Bandwidths

To obtain the operational bandwidth of the circular HIS of Section 2.2 when used as a ground plane, the spiral element of Fig. 4.10 is placed at a very small height above the surface, as illustrated in Fig. 4.11. The diameter D of the spiral is then varied and the frequency interval over which the return loss is below -10 dB is considered to be the operational bandwidth of the circular HIS [11]. The number of turns of each arm is maintained at two; however, the rate of a expansion changes in each case. If a varies from 0.25 cm to 0.5 cm, the diameter of the spiral increases from 1.5 cm to 2.2 cm; the spiral element is then located at a height 0.005λ above the circular HIS, where λ is the wavelength at 3.5 GHz. The input impedance of the lumped port is maintained at 50 ohms throughout the simulations. Fig. 4.12 exhibits the return loss of spiral elements of different spiral diameters, and it indicates that the -10 dB

operational BW is 44% at 3.5 GHz.

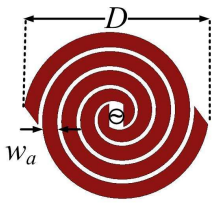

Figure 4.10: Geometry of a spiral element.

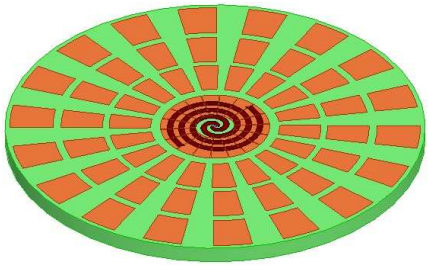

Figure 4.11: Geometry of a spiral antenna above a circular HIS of radius 8.1 cm (surface area = 210 cm^2).

To compare the operational bandwidth of the circular HIS with that of a rectangular HIS, when used as ground planes for a spiral element, a conventional rectilinear HIS with square patches (w = 0.8 cm, a = 1 cm) which has an equal surface area and an identical reflection phase under normal incidence *plane* wave illumination was designed. It should be noted that the reflection phases of the circular and rectangular HISs are obtained under different types of wave illuminations. The spiral was then located at the same height (0.005λ at 3.5 GHz) above it, as shown in Fig. 4.13, and its -10 dB operational BW of 28% at 3.5 GHz is displayed in Fig. 4.14. Thus the operational BW of the circular HIS of Fig. 4.11 for spiral elements is about 16% greater than that of the rectangular HIS of Fig. 4.13. Simulations also indicate that a spiral element has a wider operational BW above a circular HIS compared to the

corresponding rectangular HIS with an identical surface area, regardless of the height of the elements or the size of the HIS. For example, the operational BW of the spiral above the circular HIS of Fig. 4.11 with only three rings and rectangular HIS of Fig. 4.13 (with an identical surface area as the circular HIS with three rings) are 39% and 25%, respectively.

Another figure-of-merit that illustrates the superior performance of the Fig. 4.11 design over that of Fig. 4.13 is the fractional bandwidth. Fig. 4.15 indicates that the -10 dB fractional bandwidth of the spiral element above a circular HIS is wider than that above the rectangular HIS. For example, at 3.5 GHz, the fractional bandwidth of the same spiral antenna ($D/\lambda = 0.14$) is 24% and 13.7% above the circular and rectangular HIS, respectively. The return losses of the spiral and loop element are illustrated and compared in Fig. 4.16 when each is located at the same height above a circular HIS. At 3.5 GHz, the fractional bandwidth of the spiral ($D/\lambda = 0.12$) is 18%, which is 7% wider than that of the loop ($C/\lambda = 0.3$).

4.2.2 Gain Pattern

To examine the superiority of the azimuthal ϕ periodicity of the HIS ground plane, the gain of the spiral was examined. The simulated gain patterns are displayed in Fig. 4.17.

Based on *image* theory, the gain of any radiator above a PMC ground plane should be 3 dB greater than that of the radiator in free space. The broadside gain of the spiral of this design in free space is about 2.5 dB; hence, its gain should be about 5.5 dB when located above an ideal PMC surface (Perfect H boundary condition). As it is indicated in Fig. 4.17, in the case of the rectangular HIS the gain is 5.5 dB (the same as for the ideal PMC ground plane). However, when the circular HIS is used as a ground plane, the broadside gain is 8 dB which is 2.5 dB higher than

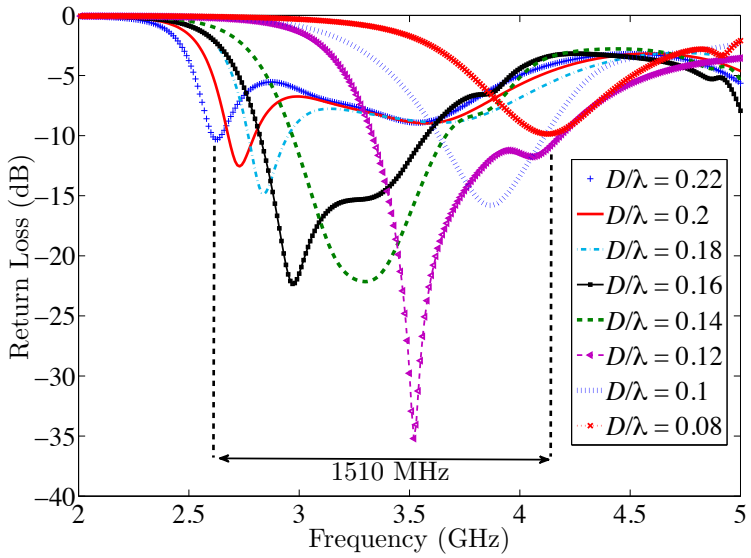

Figure 4.12: Return losses of spiral elements with different sizes located at height 0.005λ above a circular HIS.

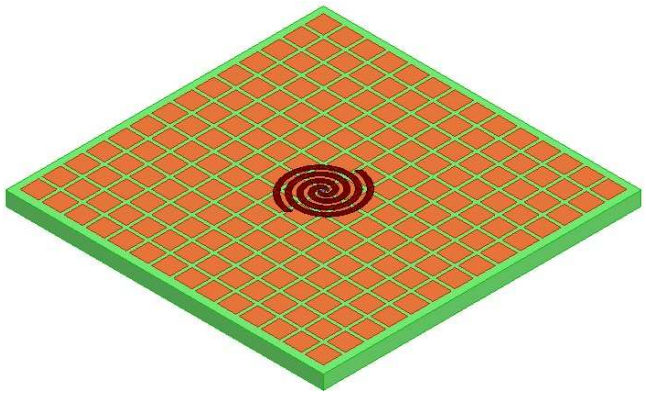

Figure 4.13: Geometry of a spiral antenna above a rectangular HIS of side 14 cm (surface area = 210 cm^2).

when a rectangular HIS or an ideal PMC ground plane is used. This increase is attributed to the phase by which the fields created by the spiral element are reflected. It should be noted that the reflection phase of Fig. 2.8 was generated for normal incidence of a cylindrical TEM^z wave. Although all of the four rings are adjusted to have the same reflection characteristic under normal illumination, they do not have the same reflection characteristic when a localized source is placed at the center and small height above the ground plane; thus each ring is illuminated at a different incidence angle. Since the texture of the surface and the incidence angle varies in the radial direction, the fields reflected from different parts of the surface possess variable phase such that it leads to a constructive interference which ultimately culminates in a stronger field intensity in the broadside direction. A method to characterize the reflection phase of a circular HIS under the illumination of a localized source is outlined in [36]. Thus, similar to loop antennas, spiral elements also benefit from the constructive radial phase profile of the circular high impedance surface which leads to an additional 2.5 dB gain increase. The broadside gains of the spiral element, when it is located above a circular HIS, rectangular HIS and an ideal PMC ground plane, are displayed and compared in Fig. 4.18. The superiority in gain of the spiral element above the circular HIS, over the entire frequency range, is evident.

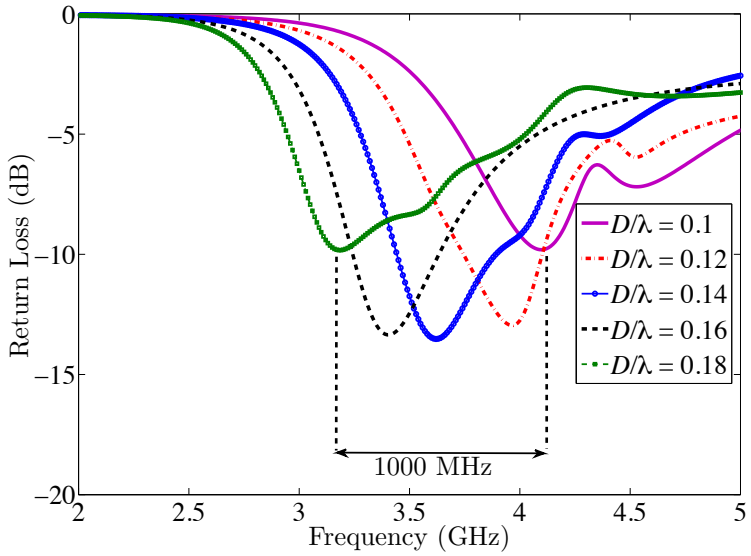

Figure 4.14: Return losses of spiral antennas with different sizes located above the rectangular HIS.

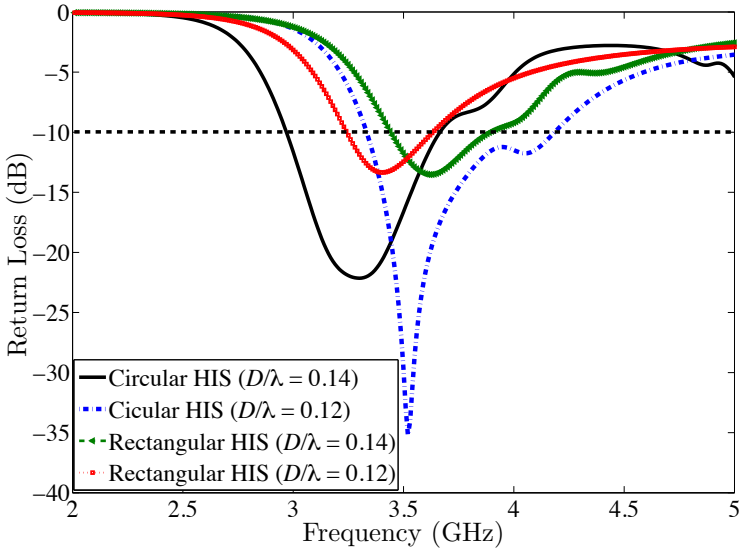

Figure 4.15: Comparison between fractional bandwidths of spiral elements when each is located above circular and rectangular HIS.

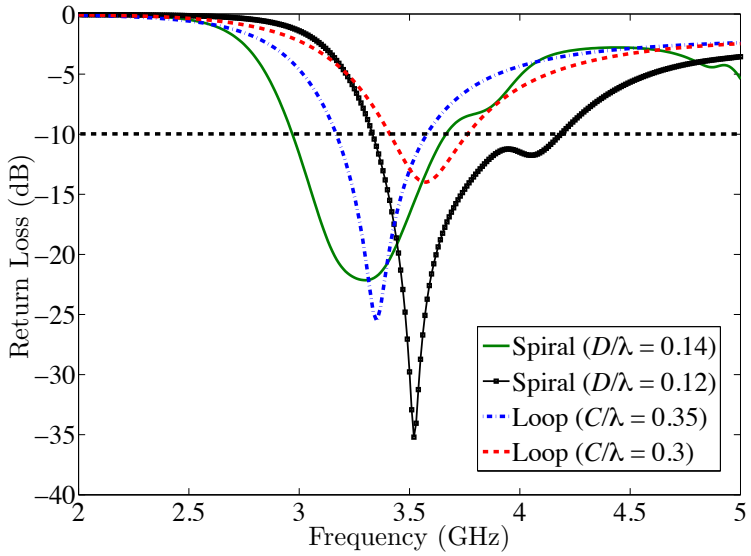

Figure 4.16: Comparison of fractional bandwidths of spiral and loop elements when each is located above a circular HIS.

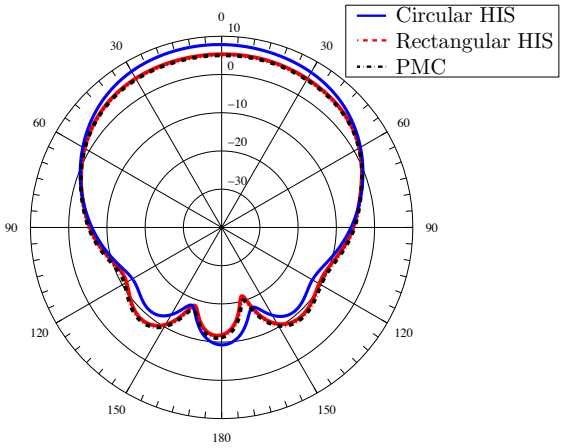

Figure 4.17: Gain patterns of spiral antenna at a height of 0.005λ above circular HIS, rectangular HIS and PMC ground plane at 3.5 GHz.

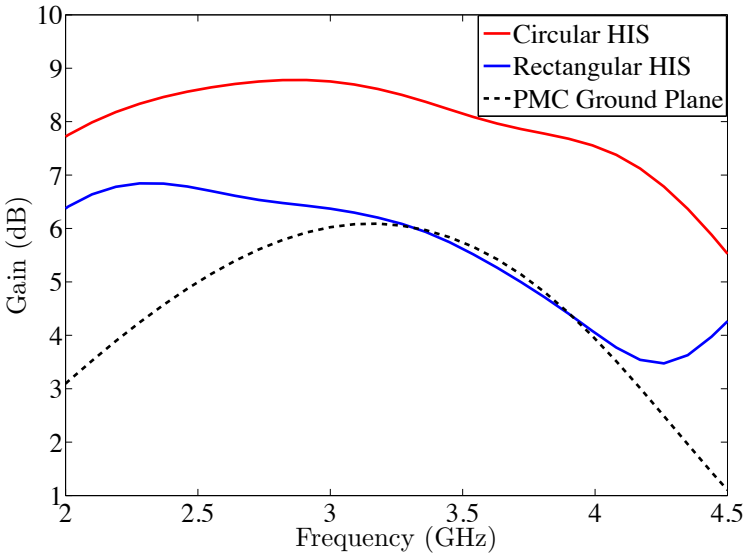

Figure 4.18: Broadside gain of a spiral antenna at a height of 0.005λ (@3.5 GHz) above a circular HIS, rectangular HIS and a PMC ground plane.

Chapter 5

SPHERICAL HIGH IMPEDANCE SURFACES

Another area of interest which has also attracted intense interest in recent years is flexible electronic devices. The extensive demand for such radio systems, inspired many antenna engineers to design conformal radiating components including antenna ground planes [48]. The overlap between the low-profile and conformal requirements gives birth to the third research area of conformal HIS ground planes [28]. In this Chapter a spherical curvature is introduced to the flat circular HIS of Chapter 2 and its impact is examined.

5.1 Curvature Impact

Fig. 2.4 displays the top view along with the design parameters of a flat HIS with circular periodicity whose design procedure is provided in [36]. The design strategy of such surfaces is based on the illumination of the individual rings with cylindrical TEM^z wave and adjusting the patch sizes such that all rings have the same zero-cross reflection phase (Fig. 2.8). The rings are then combined to form the entire circular HIS of Fig. 5.1 which eventually will have the same reflection phase as the separate rings [36, Fig. 5]. The same idea is also used to design a circular HIS with spherical curvature of Fig. 5.2. This structure is based on a grounded spherical shell of Rogers RT/ duroid 5880 with thickness of 0.623 cm. The inner radius of the spherical cap is 30 cm and the length of its outer arc is maintained equal to the radius of the flat HIS of Fig. 2.4. The same values of [36, Table. I] are used for the patch dimensions of the spherical HIS. Figure. 5.3 illustrates the reflection phase of the individual rings.

It is evident from Fig. 5.3 that although all rings are designed such that they

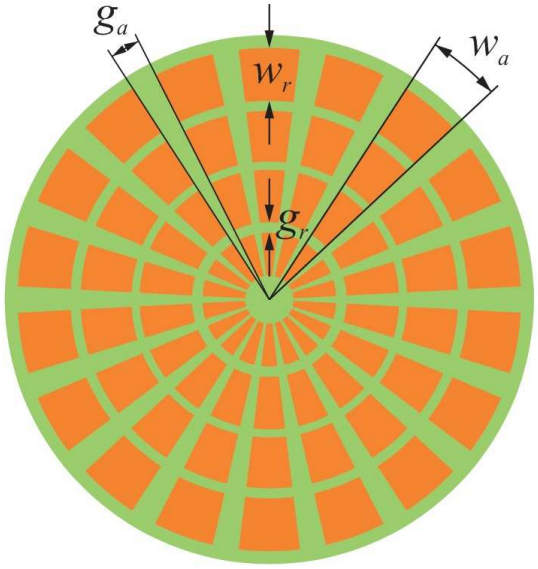

Figure 5.1: Top view of the flat circular HIS.

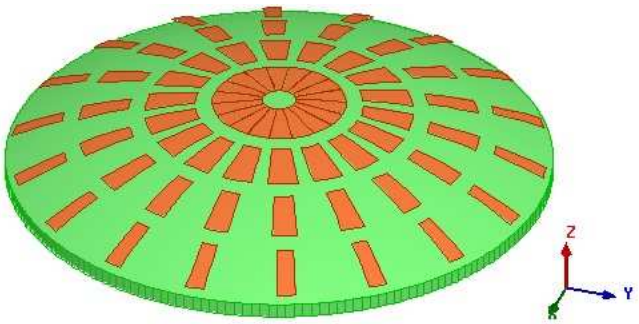

Figure 5.2: Geometry of the circular HIS with spherical curvature.

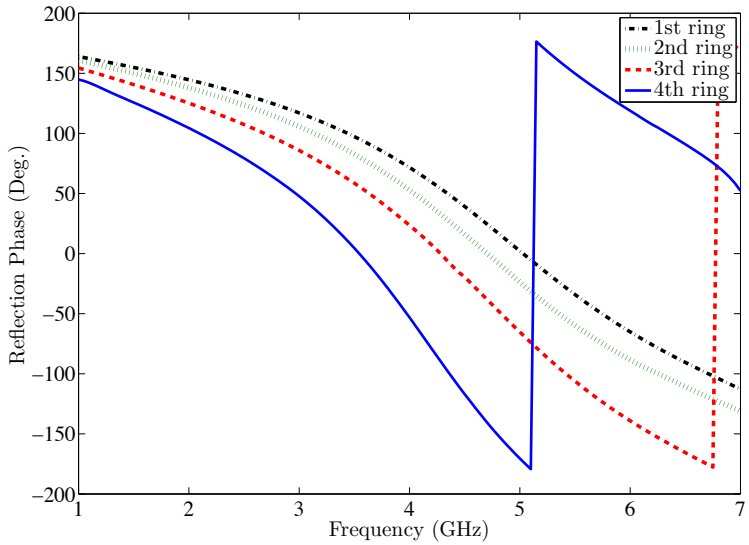

Figure 5.3: Reflection phases of the individual rings of spherical HIS of Fig. 5.4 under cylindrical TEM^z illumination.

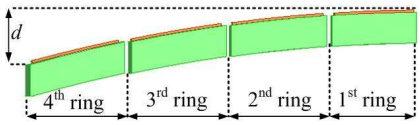

Figure 5.4: A side plane view of the rings of surface of Fig. 5.2.

introduce an identical reflection phase to the incident wave, the phase of the reflected wave front from each ring on a flat observation plane is different. This is attributed to the additional distance the wave travels to reach the surface of the outer rings compared to inner ones. Fig. 5.4 clearly illustrates the additional distance "d" that the wave travels until it impinges the surface of the 4^{th} ring compared to the 1^{st} one. Thus the patches of the spherical HIS should be redesigned such that they compensate for the phase difference introduced by the additional travel distance due to the curvature. The modified patch and gap dimensions for each ring are provided in Table 5.1, and the corresponding reflection phases of the individual rings are displayed

Table 5.1: Design parameters of the spherical circular HIS with the zero reflection phase at 4.5 GHz.

Parameter	g_a (deg)	g_r (cm)
1^{st} ring	2	1.35
2^{nd} ring	4	1.1
3^{rd} ring	10	1.1
4^{th} ring	14	1.2

in Fig. 5.5.

5.2 Curvature Limit

The design procedure of a curved circular HIS was outlined in the previous section. However, it is of interest to investigate the maximum curvature that can be applied to the flat surface and use the mentioned technique to adjust the phase response of the individual rings such that the entire surface maintains the same reflection phase. Observing the phase of the reflected wave from different rings on a flat plane, tangent to the top of the sphere, the phase of the reflected wave from the inner one (ϕ_i^r) has to be equal to the sum of the reflection phase of the outer one (ϕ_4^r) and the phase $2\beta d_{ij}$, where d_{ij} is the additional distance between rings i and j.

$$\phi_i^r = \phi_j^r + 2\beta d_{ij} \tag{5.1}$$

The minimum radius of curvature R_{min} corresponds to the maximum value of distance d between the inner and outermost rings. Solving (5.1) for d_{ij}

$$d_{ij} = \frac{\phi_i^r - \phi_j^r}{2\beta} \tag{5.2}$$

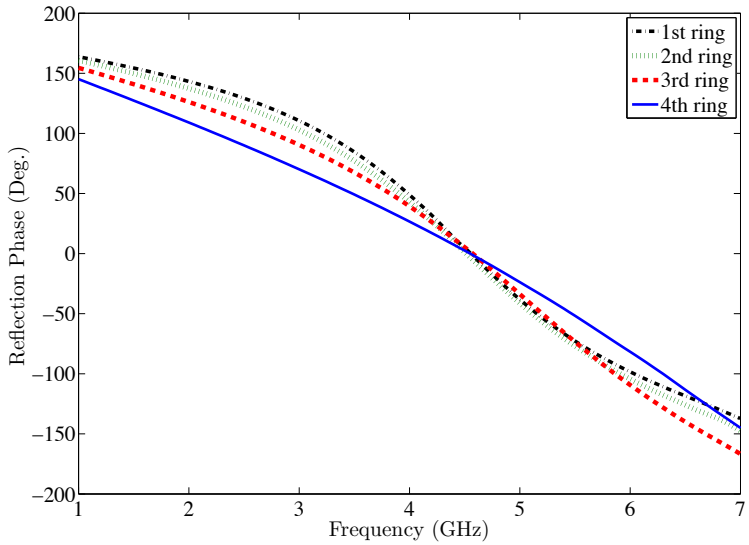

Figure 5.5: Reflection phases of the modified individual rings of spherical HIS of Fig. 5.4 under cylindrical TEM^z illumination.

indicates that the difference between the reflection phases of the inner and outermost rings limits the value of the distance d_{ij}. In Fig. 5.4, given that ϕ_1^r is zero at resonance and that the minimum value of ϕ_4^r within the same mode is $-\pi$, the maximum value of d is

$$d_{max} = \frac{\pi}{2\beta} \tag{5.3}$$

Based on the geometry of Fig. 5.6, we can write that

$$d = 2R\sin^2\left(\frac{r}{2R}\right) \tag{5.4}$$

where R and r are, respectively, the radii of curvature of the spherical HIS of Fig. 5.2 and the surface of the flat HIS of Fig. 2.4. Substituting d_{max} of (5.3) in (5.4), leads to

$$R_{min}\sin^2\left(\frac{r}{2R_{min}}\right) = \frac{\lambda}{8} \tag{5.5}$$

If the radius of curvature is larger than the radius of the flat HIS ($R >> r$), (5.5) can be approximated by

$$R_{min} = \frac{2r^2}{\lambda} \tag{5.6}$$

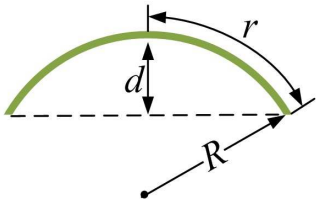

Figure 5.6: The side plane view of a spherical HIS of radius of curvature R and arc length r.

Chapter 6

ANTENNA APPLICATIONS OF SPHERICAL CHIS

As it was mentioned in Chapter 5, the spherical HIS is used as an antenna ground plane. Two curvilinear elements (loop and spiral) are located above the designed surface of Chapter 5 and the operational bandwidth of the surface for each element and also their realized gain patterns are obtained. Fig. 6.1 illustrates the geometry and design parameters of the curvilinear radiating elements.

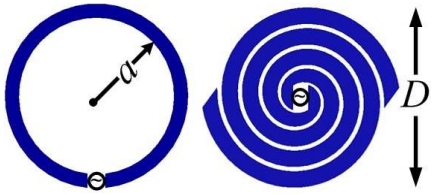

Figure 6.1: Geometry of loop and two-arm spiral elements.

6.1 Operational Bandwidth

To determine the operational bandwidth of the spherical HIS for each of the elements, they are placed in the vicinity of the ground plane, as shown in Fig. 6.2, and the sizes of the loop and spiral (a and D in Fig. 6.1) are varied. Fig. 6.3 displays the -10 dB operational bandwidth of the loop and spiral elements located at a height 0.005 λ (wavelength at 3.5 GHz) above the spherical HIS of Fig. 5.2. The operational bandwidths for the loop and spiral elements at 3.5 GHz are 21% and 28%, respectively; while those of the flat circular HIS reported in [36], [37] for the same elements are 31% and 44%, respectively. In other words the operational bandwidths of the spherical design was reduced by 10% and 16% compared to the flat design of [36] for the loop and spiral, respectively.

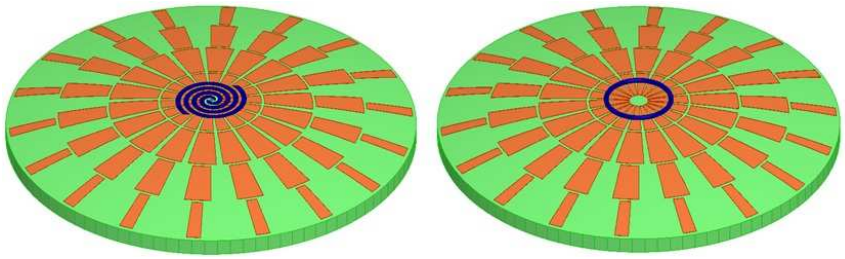

Figure 6.2: 3D CAD geometry of the curvilinear elements above the spherical HIS ground plane.

6.2 Gain Pattern

The realized gain [46] patterns of the curvilinear elements were also evaluated. Fig. 6.4 illustrates the realized gain of the loop and spiral radiators above the spherical HIS of Fig. 6.2, PMC ground plane with an identical curvature, flat circular HIS of [36] and flat PMC ground plane. The broadside gain of a loop ($C/\lambda = 0.6$) and a spiral ($D/\lambda = 0.15$) antenna in free-space is 2.5 dB and 3 dB, respectively. Due to *image* theory, a 3 dB gain enhancement is expected when the loop and spiral are placed above a flat PMC ground plane which is also indicated in Fig. 6.4; i.e., the gain of the elements has increased to 5.5 dB and 6 dB. Although the same performance is expected when these elements are placed above the circular HIS, an additional 3 dB increase is observed for both the loop and spiral, with total gains of 8.5 dB and 9 dB, respectively. As a detailed explanation is provided in [36], [49], the substantial (+3 dB) enhancement of the gain is attributed to the radial reflection phase profile along the surface of the circular HIS. Modeling and synthesizing the surface impedance based on such a reflection phase profile substantiates that the wavefronts of the curvilinear elements (loop and spiral) are reflected such that they have a constructive interference in the broadside direction, which eventually results in a 3-dB higher gain compared to a flat PMC ground plane where the wavefronts are reflected with a uniform reflection

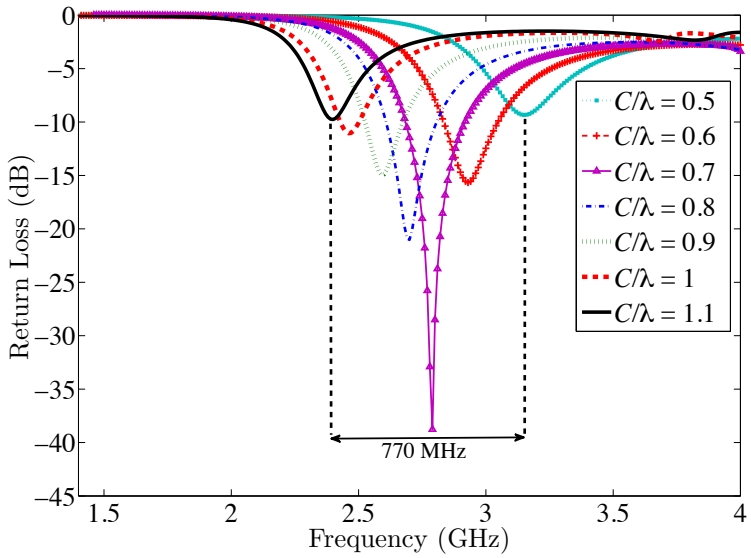

(a)

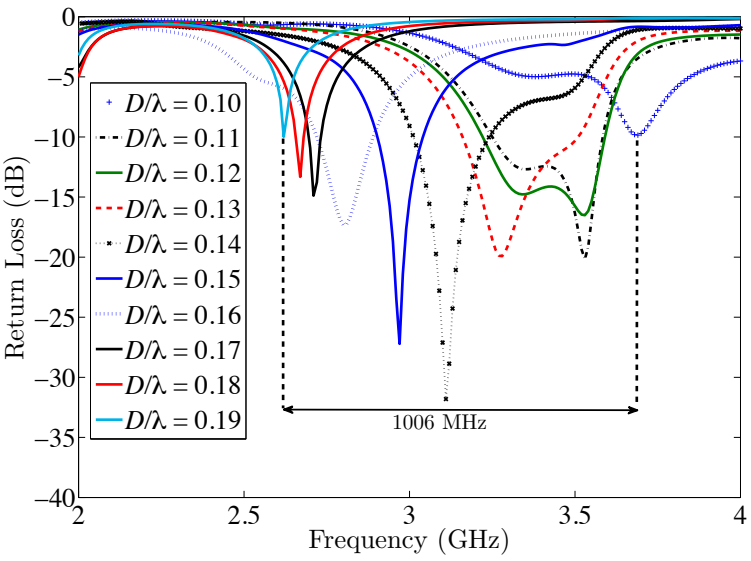

(b)

Figure 6.3: Operational bandwidth of the curvilinear element at a height of 0.005 λ above the spherical HIS: (a) Loop (b) Spiral.

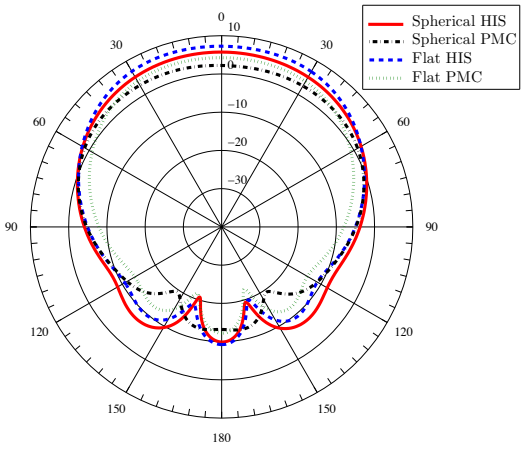

(a)

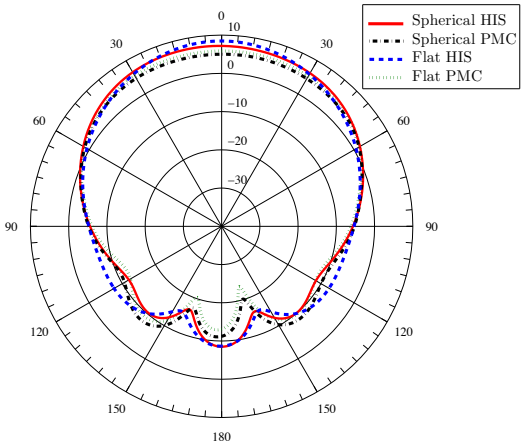

(b)

Figure 6.4: Realized gain patterns of the curvilinear elements at a height of 0.005 λ above the spherical HIS at 3 GHz: (a) Loop (b) Spiral.

phase along the surface. Introducing curvature to the antenna ground plane prompts the electromagnetic energy to scatter in non-broadside directions which results in an expected gain degradation. Thus the gain of both elements located above the spherical

HIS ground plane is about 1.5 dB lower compared to gain of the same elements above the flat circular HIS. However, the curvilinear elements above the spherical HIS still have a 3 dB higher gain than those located above a spherical PMC ground plane with an identical radius of curvature.

Chapter 7

MEASUREMENTS

7.1 Flat Circular HIS (CHIS)

7.1.1 Loop Element

To validate the simulations, the proposed circular HIS was fabricated, as shown in Fig. 7.1, and measurements were performed. To feed the radiating element from beneath the HIS, it was required to pass the inner conductor of the coaxial cable through the substrate and connect it to one of the loop terminals. The other terminal was connected to the outer conductor of the coaxial cable which itself was connected to the ground plane of the HIS. The dimensions of the loop were such that clearance holes had to be constructed on the patches of the first ring to prevent the antenna from being shorted out to them while passing the feed wires through the substrate. However, simulations indicated that the performance of the surface with two clearance holes on the first ring deviates from what it was expected to be. Thus, the holes where constructed close to the metallic patches and two parallel wires were used to connect the conductors of the coaxial cable to the terminals of the loop. Fig. 7.2 illustrates the loop antenna along with the parallel wires which connect its input terminals to the source. A plastic film of thickness 1.15 mm, with a relative permittivity of approximately unity, is also used to provide the desired height above the surface.

The return loss of two different loops with radii of 3 cm and 2.7 cm were measured. The input impedance and the pattern of the realized gain for the later case were also measured. The simulations and measurements are displayed and compared in Figs. 7.3 and 7.4. An excellent agreement between them is indicated.

Figure 7.1: Fabricated circular HIS with the loop antenna at a height of 0.01λ.

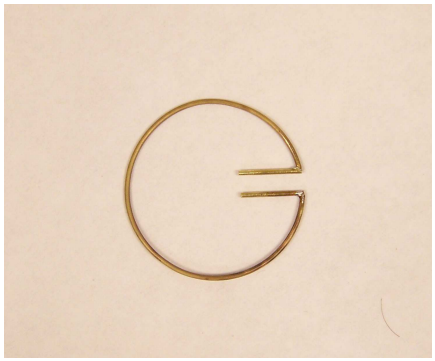

Figure 7.2: Geometry of the loop antenna along with the parallel wires which were used to avoid the creation of clearance holes on the metal patches.

7.1.2 Spiral Element

To verify the simulation data, measurements were performed. A two-arm spiral element with two turns and an expansion rate of 0.45 cm was etched on copper tape and adhered to a thin dielectric film of 0.05 mm thickness. Fig. 7.5 displays the fabricated circular HIS with the spiral element above it.

Since the coaxial feed-line is unbalanced and a spiral is a balanced element, a balun is needed to make the radiating system balanced [46]. However, the bandwidth

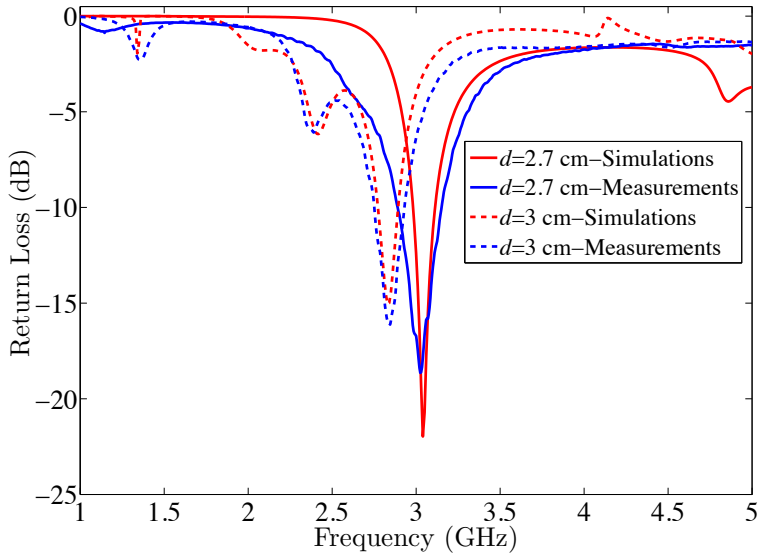

(a)

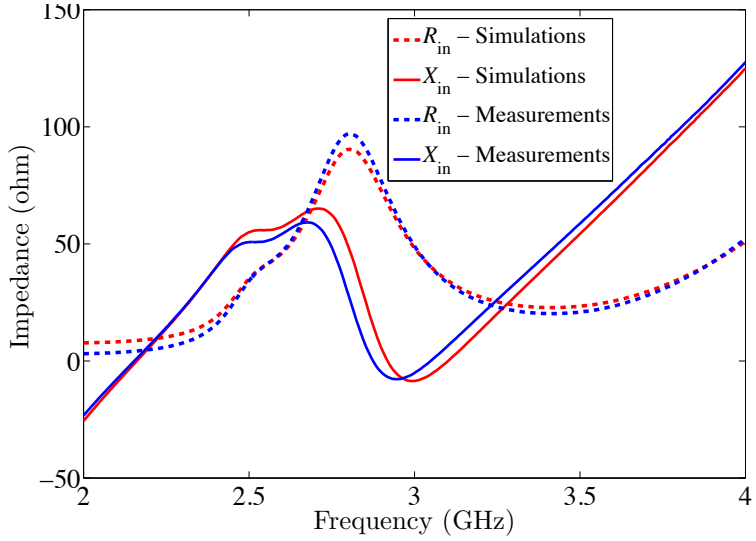

(b)

Figure 7.3: Simulations and measurements of the loop element above the flat CHIS: (a) Return loss (b) Input impedance

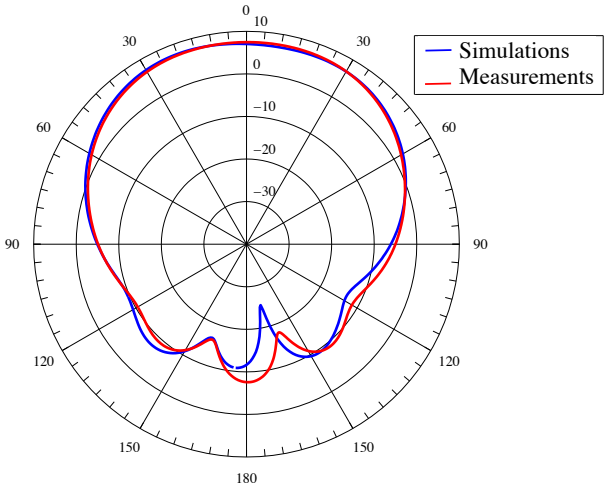

Figure 7.4: Simulations and measurements of the loop element above the flat CHIS: Gain pattern at 3 GHz.

of the balun can be a limiting factor; so a wideband balun is required. It is also more convenient to feed the element from underneath the ground plane, so that the impact of the coaxial cable on the radiation pattern is minimal. Therefore, it was decided to taper the outer conductor of the coaxial cable, as proposed in [50], to design a wideband balun. The balun was passed through a clearance hole made at the center of circular HIS. The tapered and inner conductors were then connected to each arm of the spiral. The CAD geometry of the wideband balun is shown in Fig. 7.6.

Fig. 7.7 displays the return loss and realized gain patterns of the spiral antenna at the resonant frequency of 2.7 GHz. The maximum realized gain is 8 dB. Although there are some slight differences in the back angular region, due to the inaccuracy in the fabrication process of the balun, an excellent agreement between simulations and measurements is indicated over the entire angular space. As mentioned earlier, the 3-dB axial ratio bandwidths is maintained at 11%.

(a)

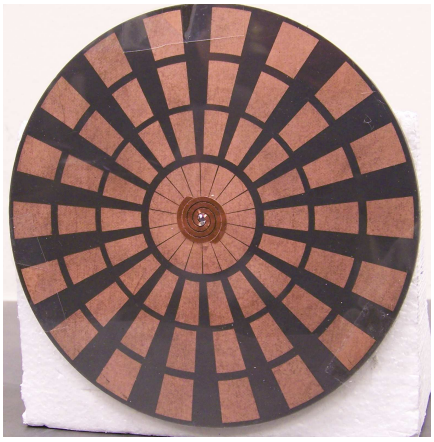

(b)

Figure 7.5: Fabricated prototype: (a) Spiral element (b) Circular HIS.

Figure 7.6: Tapered coaxial cable used as a wideband balun to feed the spiral.

7.2 Spherical CHIS

To validate the simulations, a spherical HIS was fabricated and measurements were conducted. It should be noted that Rogers RT/duroid 5880 was used throughout the simulations in the previous sections; however ABS plastic ($\epsilon_r = 2.75$, $\tan\delta = 0.004$) is used for fabrication as Rogers 5880 was not available with the desired thickness. The dielectric characteristics of the substrate of the HIS is modified accordingly in simulations to make the comparison more realistic. Figure. The fabricated spherical

HIS is illustrated in Fig. 7.10 and the loop element located above it. The following steps describe the fabrication process of the spherical HIS prototype.

1. The spherical shell was carved out of an ABS dielectric block using a Computer Numerical Control (CNC) machine.

2. The back of the spherical shell was covered with copper paint as displayed in Fig. 7.8.

3. A mask of the patches on Vinyl plastic was prepared and placed on the top surface of the spherical shell and it was painted with copper as displayed in Fig. 7.9.

4. Adhering the copper tape on a thin film, print the negative mask of the loop element on it and use etchant to remove the extra portion of the copper.

Figure. 7.11 illustrates the simulated and measured return loss and realized gain patterns of the loop element above the spherical HIS. It should be noted that to make the comparison fair, the electrical properties of the ABS plastic and copper paint were implemented in the simulation models. An excellent agreement is observed between simulations and measurements.

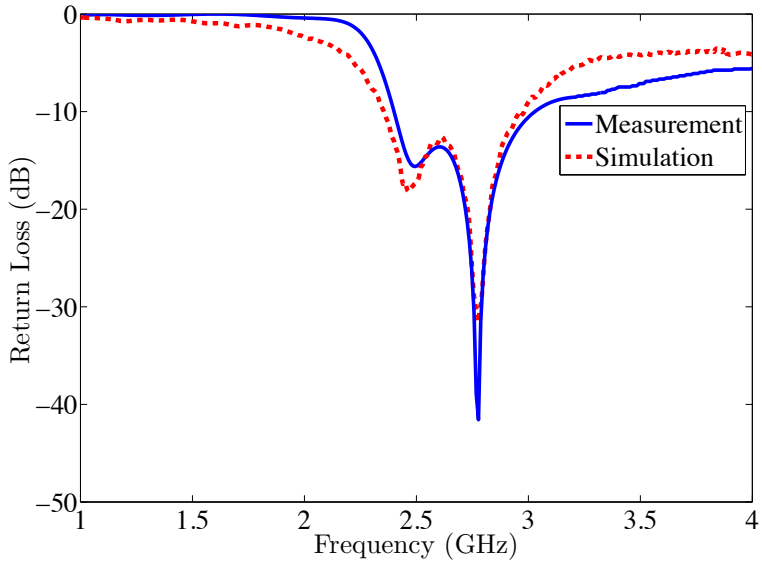

(a)

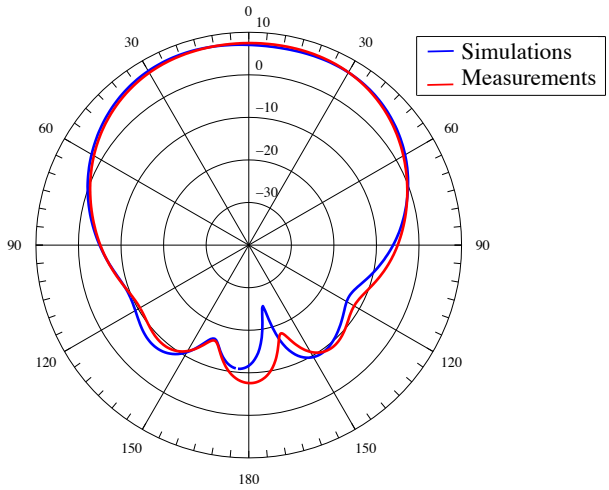

(b)

Figure 7.7: Simulations and measurements of the spiral element above the flat CHIS: (a) Return loss (b) Realized gain pattern at 2.7 GHz.

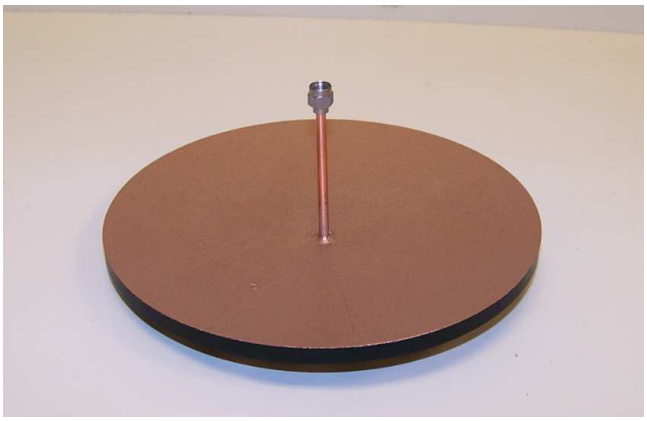

Figure 7.8: Covering the back of the spherical shell with copper paint.

(a)

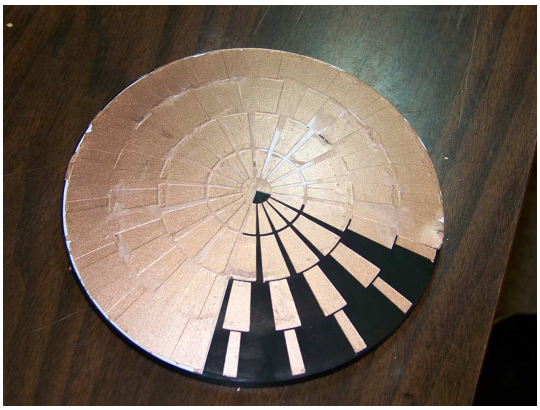

(b)

Figure 7.9: Vinyl mask and copper paint used on the surface of the spherical shell.

(a)

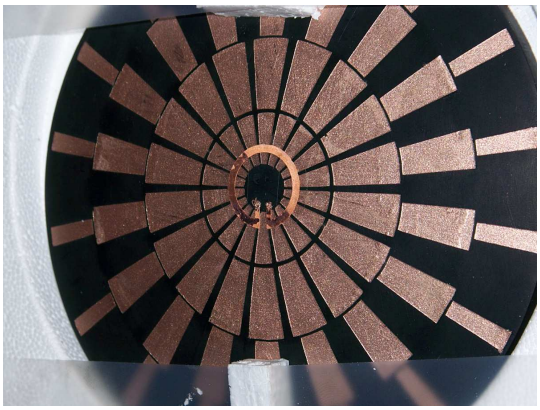

(b)

Figure 7.10: Fabricated prototype: (a) Spherical HIS ground plane (b) Loop element above spherical HIS.

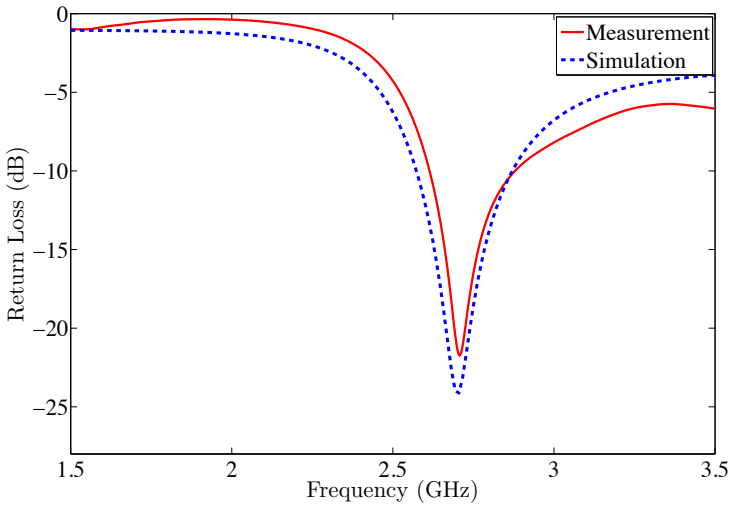

(a)

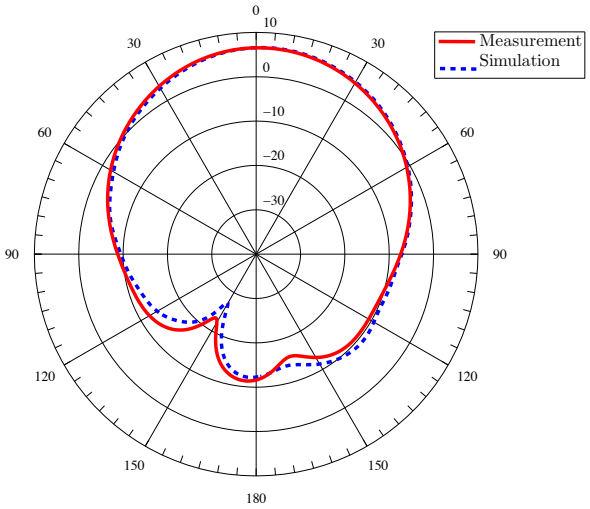

(b)

Figure 7.11: Simulations and measurements of the loop element above spherical HIS: (a) Return loss (b) Realized gain pattern.

Chapter 8

CONCLUSIONS AND FUTURE WORK

8.1 Conclusions

In this dissertation, a procedure to design a wideband circularly symmetric high impedance surface was proposed. The basic design principle of such surfaces is to illuminate individual rings with a cylindrical TEM^z wave and adjust the patch sizes such that all the rings have the same reflection characteristic. The rings are then combined to form the HIS ground plane and the surface is illuminated with the same cylindrical TEM^z wave. Simulations indicate that the entire surface has a very similar reflection property as the individual rings.

Two models were developed to analyze the reflection characteristics of the surface under normal incidence of a cylindrical TEM^z wave. The *quasi-static* model was simpler but accurate only within the low frequency ranges for certain gap sizes between the metallic patches. For the *wideband* model, the impact of the higher order modes was taken into account, which made the results more accurate at higher frequency ranges and for wider gaps between the metallic patches.

The proposed HIS was then used as a ground plane for curvilinear radiating elements and the figures-of-merit were compared with those of the rectangular HIS ground plane. It was shown that the ϕ-direction periodicity of the circular HIS interacts more efficiently with the electromagnetic waves radiated by a loop element compared with a rectangular HIS. The superiorities of the circular HIS over rectangular HIS, when used as a ground plane for loop antennas, can be summarized as follows:

1. The operational bandwidth of the circular surface is about 10% wider than that of the rectangular surface.

2. The gain patterns of the loop antenna above a circular HIS on different elevation ϕ planes are more symmetric than the gain pattern when the antenna is located above a rectangular HIS.

3. Because of the radial reflection phase profile introduced by the circular HIS when illuminated by a loop radiating element, the gain of the loop is higher when it is located above the circular HIS compared to the rectangular HIS.

Furthermore the circular HIS surface was used as a ground plane for a spiral element. As expected, a wider operational bandwidth was observed compared to rectangular HIS. The gain of a spiral element is also enhanced when it is located above a circular HIS.

These attractive features of a circular HIS with curvilinear radiating elements are intuitively attributed to the matching of the curvature of the radiating element wavefront to the circular periodicity of the HIS patches, which leads to a more efficient coupling between the dominant ϕ-polarized electric field radiated by the curvilinear elements and circular ϕ-periodicity of the HIS.

In the last sections of this dissertation, a novel circular HIS with spherical curvature was designed. The proposed HIS was used as antenna ground plane for loop and spiral elements, and its performance was compared with a flat circular HIS. As expected, due to the ground plane curvature, the simulations indicate that the operational bandwidth decreases by 10% and 16% for the loop and spiral, respectively. Additionally due to the curvature, the gain of the antenna elements degrades by 1.5 dB as the waves are scattered toward non-broadside directions. However, the broadside gain of the curvilinear element above the spherical HIS is still 3 dB higher

compared to when it is placed above a spherical PMC ground plane with the same curvature.

The proposed HISs (flat and spherical) were ultimately fabricated and measurements were performed to validate the simulations. It was shown that the measurements were in excellent agreement with the simulations.

8.2 Future Work

In this dissertation we attempted to design a circular HIS which has a superior performance as a ground plane for curvilinear elements; however, there is still more room for advancements.

- One of the interesting features of the designed circular HIS is the substantial 3-dB gain increase when it is used as ground plane for curvilinear elements. It would be a rewarding challenge to modify the patch design of the circular HIS to optimize the radial phase profile along the surface and further improve the gain of the curvilinear elements and also investigate the maximum gain value that can be achieved through this design strategy.

- Another area of interest is to design a dual band circular HIS. As it is mentioned in Chapter 2, for a wideband design of the circular HIS, the rings are adjusted individually such that all of them have an in-phase reflection phase at the same frequency and they are then combined to form the entire circular HIS ground plane. However, for a dual band HIS, the inner rings which are closer to the radiating element should be designed such that they resonate at the higher frequency and the outer ones which are further should resonate at the lower frequency as illustrated in Fig. 8.1. The two parts of Fig. 8.1 are then combined to form the entire dualband surface as displayed in Fig. 8.2.

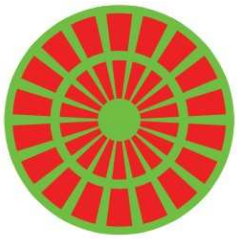

(a)

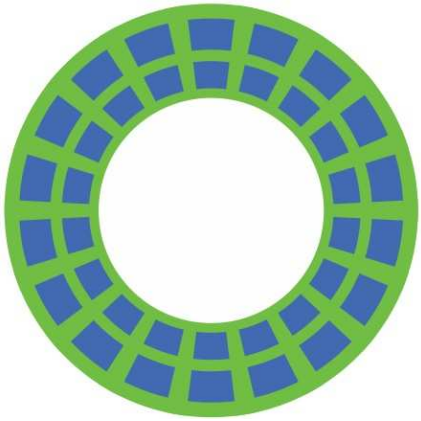

(b)

Figure 8.1: Different sections of the dual band circular HIS: (a) Higher frequency (b) Lower frequency.

- In most of the applications where spiral antennas are used, a circular polarization is desired. The circular HIS proposed in this dissertation was optimized with respect to the reflection phase and operational bandwidth. The 3-dB axial ratio bandwidth of the spiral element above the circular HIS of this dissertation was 11%; it would be interesting to investigate a design strategy to optimize the circular HIS with respect to the axial ratio.

- In most of the previous investigation, patch elements are placed above the HISs and their performance is studied. As the circular HIS of this dissertation is

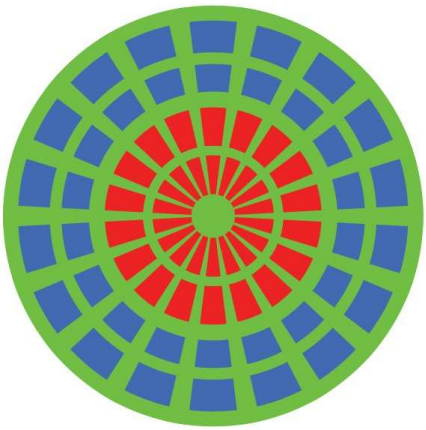

Figure 8.2: Top view of the entire dualband surface.

designed for curvilinear elements, it would be of interest to place a circular patch above the circular and rectangular HISs (as illustrated in Fig. 8.3) to compare their radiation characteristics and validate that circular HIS are superior ground planes for such radiating elements.

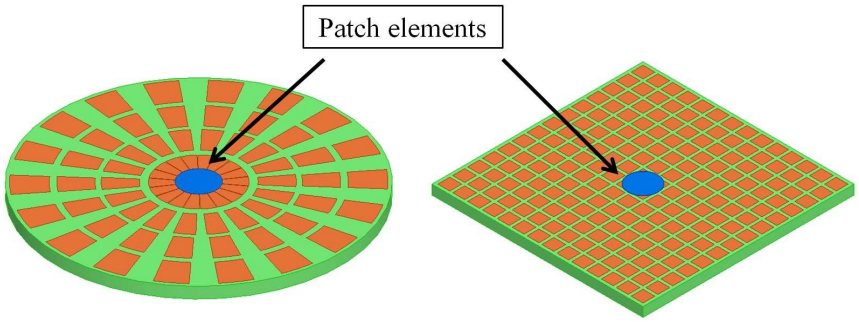

Figure 8.3: Top view of the flat circular HIS.

- A spiral element and a wideband balun can be fabricated and placed above the spherical HIS to perform measurements and verify simulations.

REFERENCES

[1] D. Sievenpiper, "High-impedance electromagnetic surfaces", Ph. D. dissertation, *Electrical Engineering Department University of California, Los Angeles, Los Angeles, Calif, USA*, 1999.

[2] F. Yang and Y. Rahmat-Samii, *Electromagnetic band gap structures in antenna engineering*. Cambridge university press Cambridge, UK, 2009.

[3] B. A. Munk, *Finite Antenna Arrays and FSS*. John Wiley & Sons, 2003.

[4] D. F. Sievenpiper, "Artificial impedance surfaces for antennas," *Modern Antenna Handbook*, pp. 737–777, 2008.

[5] M. Gustafsson and D. Sjoberg, "Physical bounds and sum rules for high-impedance surfaces," *IEEE Transactions on Antennas and Propagation*, vol. 59, no. 6, pp. 2196–2204, 2011.

[6] M. F. Samani and R. Safian, "On bandwidth limitation and operating frequency in artificial magnetic conductors," *IEEE Antennas and Wireless Propagation Letters*, vol. 9, pp. 228–231, 2010.

[7] S. Tretyakov, *Analytical Modeling in Applied Electromagnetics*. Artech House, 2003.

[8] O. Luukkonen, C. Simovski, G. Granet, G. Goussetis, D. Lioubtchenko, A. V. Raisanen, and S. A. Tretyakov, "Simple and accurate analytical model of planar grids and high-impedance surfaces comprising metal strips or patches," *IEEE Transactions on Antennas and Propagation*, vol. 56, no. 6, pp. 1624–1632, 2008.

[9] R. Rodriguez-Berral, F. Medina, F. Mesa, and M. Garcia-Vigueras, "Quasi-analytical modeling of transmission/reflection in strip/slit gratings loaded with dielectric slabs," *IEEE Transactions on Microwave Theory and Techniques*, vol. 60, no. 3, pp. 405–418, 2012.

[10] R. Rodriguez-Berral, C. Molero, F. Medina, and F. Mesa, "Analytical wideband model for strip/slit gratings loaded with dielectric slabs," *IEEE Transactions on Microwave Theory and Techniques*, vol. 60, no. 12, pp. 3908–3918, 2012.

[11] F. Yang and Y. Rahmat-Samii, "Reflection phase characterizations of the ebg ground plane for low profile wire antenna applications," *IEEE Transactions on Antennas and Propagation*, vol. 51, no. 10, pp. 2691–2703, 2003.

[12] A. Vallecchi, J. R. De Luis, F. Capolino, and F. De Flaviis, "Low profile fully planar folded dipole antenna on a high impedance surface," *IEEE transactions on antennas and propagation*, vol. 60, no. 1, pp. 51–62, 2012.

[13] M. Z. Azad and M. Ali, "Novel wideband directional dipole antenna on a mushroom like ebg structure," *IEEE Transactions on antennas and propagation*, vol. 56, no. 5, pp. 1242–1250, 2008.

[14] C. A. Balanis, *Advanced Engineering Electromagnetics*. John Wiley & Sons, 2012.

[15] L. Akhoondzadeh-Asl, D. J. Kern, P. S. Hall, and D. H. Werner, "Wideband dipoles on electromagnetic bandgap ground planes," *IEEE Transactions on Antennas and Propagation*, vol. 55, no. 9, pp. 2426–2434, 2007.

[16] H. Mosallaei and K. Sarabandi, "Antenna miniaturization and bandwidth enhancement using a reactive impedance substrate," *IEEE Transactions on Antennas and Propagation*, vol. 52, no. 9, pp. 2403–2414, 2004.

[17] T. Nakamura and T. Fukusako, "Broadband design of circularly polarized microstrip patch antenna using artificial ground structure with rectangular unit cells," *IEEE Transactions on Antennas and Propagation*, vol. 59, no. 6, pp. 2103–2110, 2011.

[18] D. J. Kern, D. H. Werner, A. Monorchio, L. Lanuzza, and M. J. Wilhelm, "The design synthesis of multiband artificial magnetic conductors using high impedance frequency selective surfaces," *IEEE Transactions on Antennas and Propagation*, vol. 53, no. 1, pp. 8–17, 2005.

[19] T. Liang, L. Li, J. A. Bossard, D. H. Werner, and T. S. Mayer, "Reconfigurable ultra-thin ebg absorbers using conducting polymers," in *2005 IEEE Antennas and Propagation Society International Symposium*, vol. 2B, July 2005, pp. 204–207.

[20] R. Coccioli, F.-R. Yang, K.-P. Ma, and T. Itoh, "Aperture-coupled patch antenna on uc-pbg substrate," *IEEE Transactions on Microwave Theory and Techniques*, vol. 47, no. 11, pp. 2123–2130, 1999.

[21] B.-q. Lin, Q.-r. Zheng, and N.-c. Yuan, "A novel planar pbg structure for size reduction," *IEEE Microwave and Wireless Components Letters*, vol. 16, no. 5, pp. 269–271, 2006.

[22] A. Tayebi, P. Roy Paladhi, L. Udpa, and S. Udpa, "A novel time reversal based microwave imaging system," *Progress In Electromagnetics Research C*, vol. 62, pp. 139–147, 2016.

[23] A. Tayebi, P. Chahal, L. Udpa, and S. S. Udpa, "Nondestructive testing of dielectric materials using an active reflecting microwave array," *Materials Evaluation*, vol. 74, no. 12, pp. 1684–1691, 2016.

[24] A. Tayebi, J. Tang, P. Roy Paladhi, L. Udpa, and S. S. Udpa, "Design and development of an electrically-controlled beam steering mirror for microwave tomography," in *AIP Conference Proceedings*. AIP, 2015, pp. 501–508.

[25] J. Tang, A. Tayebi, S. S, E. J. Rothwell, and A. Temme, "A dual-band tunable reflectarray," in *Antennas and Propagation (APSURSI), 2014 IEEE International Symposium*. IEEE, 2014, pp. 1033–1034.

[26] A. Tayebi, J. Tang, P. Roy Paladhi, L. Udpa, S. S. Udpa, and E. J. Rothwell, "Dynamic beam shaping using a dual-band electronically tunable reflectarray antenna," *IEEE Transactions on Antennas and Propagation*, vol. 63, no. 10, pp. 4534–4539, 2015.

[27] A. Tayebi, "Microwave imaging using a tunable reflectarray antenna and superradiance in open quantum systems," Ph.D. dissertation, Michigan State University, 2017.

[28] A. C. Durgun, C. A. Balanis, and C. R. Birtcher, "Reflection phase characterization of curved high impedance surfaces," *IEEE Transactions on Antennas and Propagation*, vol. 61, no. 12, pp. 6030–6038, 2013.

[29] J. Sarrazin, A.-C. Lepage, and X. Begaud, "Circular high-impedance surfaces characterization," *IEEE Antennas and Wireless Propagation Letters*, vol. 11, pp. 260–263, 2012.

[30] N. Llombart, A. Neto, G. Gerini, and P. de Maagt, "Planar circularly symmetric ebg structures for reducing surface waves in printed antennas," *IEEE transactions on antennas and propagation*, vol. 53, no. 10, pp. 3210–3218, 2005.

[31] A. Neto, N. Llombart, G. Gerini, and P. De Maagt, "On the optimal radiation bandwidth of printed slot antennas surrounded by ebgs," *IEEE transactions on antennas and propagation*, vol. 54, no. 4, pp. 1074–1083, 2006.

[32] M. Ettorre, S. Bruni, G. Gerini, A. Neto, N. Llombart, and S. Maci, "Sector pcs-ebg antenna for low-cost high-directivity applications," *IEEE Antennas and Wireless Propagation Letters*, vol. 6, pp. 537–539, 2007.

[33] M. SalarRahimi, J. Rashed-Mohassel, and M. Edalatipour, "Radiation properties enhancement of a gsm/wlan microstrip antenna using a dual band circularly symmetric ebg substrate," *IEEE Transactions on Antennas and Propagation*, vol. 60, no. 11, pp. 5491–5494, 2012.

[34] T. A. Denidni, Y. Coulibaly, and H. Boutayeb, "Hybrid dielectric resonator antenna with circular mushroom-like structure for gain improvement," *IEEE Transactions on Antennas and Propagation*, vol. 57, no. 4, pp. 1043–1049, 2009.

[35] D. H. Werner, "An exact integration procedure for vector potentials of thin circular loop antennas," *IEEE Transactions on Antennas and Propagation*, vol. 44, no. 2, pp. 157–165, 1996.

[36] M. A. Amiri, C. A. Balanis, and C. R. Birtcher, "Analysis, design, and measurements of circularly symmetric high-impedance surfaces for loop antenna applications," *IEEE Transactions on Antennas and Propagation*, vol. 64, no. 2, pp. 618–629, 2016.

[37] "Gain and bandwidth enhancement of spiral antenna using circularly symmetric his," *IEEE Letters on Antenna and Wireless Propagation*, vol. 16, no. 4, pp. 1080 – 1083, 2016.

[38] C. A. Balanis, M. A. Amiri, A. Modi, S. Pandi, and C. R. Birtcher, "Applications of amc-based impedance surfaces," *Applied Metamaterial*, vol. 5, no. 3, pp. 1 – 15, 2018.

[39] M. A. Amiri, C. A. Balanis, and C. R. Birtcher, "Applications of circularly symmetric high impedance surfaces for spiral antennas," in *Antennas and Propagation (APSURSI), 2016 IEEE International Symposium*. IEEE, 2016, pp. 1947–1491.

[40] M. Grelier, C. Djoma, M. Jousset, S. Mallégol, A.-C. Lepage, and X. Begaud, "Axial ratio improvement of an archimedean spiral antenna over a radial amc reflector," *Applied Physics A*, vol. 109, no. 4, pp. 1081–1086, 2012.

[41] A. M. Mehrabani and L. Shafai, "An extremely low-profile offset-fed curl antenna over an amc ground," *Microwave and Optical Technology Letters*, vol. 53, no. 5, pp. 1036–1041, 2011.

[42] M. A. Amiri, C. A. Balanis, and C. R. Birtcher, "Reflection phase characterization of spherical high impedance surfaces with circular periodicity," in *Antennas and Propagation (APSURSI), 2017 IEEE International Symposium*. IEEE, 2017, pp. 1947–1491.

[43] S. Ramo, J. R. Whinnery, and T. Van Duzer, *Fields and waves in communication electronics*. John Wiley & Sons, 2008.

[44] R. Rodriguez-Berral, C. Molero, F. Medina, and F. Mesa, "Analytical wideband model for strip/slit gratings loaded with dielectric slabs," *IEEE Transactions on Microwave Theory and Techniques*, vol. 60, no. 12, pp. 3908–3918, 2012.

[45] M. Kobayashi, "Longitudinal and transverse current distributions on microstriplines and their closed-form expression," *IEEE transactions on microwave theory and techniques*, vol. 33, no. 9, pp. 784–788, 1985.

[46] C. A. Balanis, *Antenna Theory: Analysis and Design*. John Wiley & Sons, 2016.

[47] C. R. Simovski, P. de Maagt, and I. V. Melchakova, "High-impedance surfaces having stable resonance with respect to polarization and incidence angle," *IEEE Transactions on Antennas and Propagation*, vol. 53, no. 3, pp. 908–914, 2005.

[48] A. C. Durgun, C. A. Balanis, C. R. Birtcher, and D. R. Allee, "Design, simulation, fabrication and testing of flexible bow-tie antennas," *IEEE Transactions on Antennas and Propagation*, vol. 59, no. 12, pp. 4425–4435, 2011.

[49] M. A. Amiri, C. A. Balanis, and C. R. Birtcher, "Notable gain enhancement of curvilinear elements using a circular his ground plane," in *Antennas and Propagation (APSURSI), 2017 IEEE International Symposium*. IEEE, 2017, pp. 1671–1672.

[50] J. Duncan and V. Minerva, "100:1 bandwidth balun transformer," *Proceedings of the IRE*, vol. 48, no. 2, pp. 156–164, 1960.